International Journal of Fatigue 167 (2023) 107353

Contents lists available at ScienceDirect

International Journal of Fatigue

journal homepage: www.elsevier.com/locate/ijfatigue

Size effect of steel fiber–reinforced concrete cylinders under compressive fatigue loading: Influence of the mesostructure

Dorys C. González [a,*], Álvaro Mena [a], Gonzalo Ruiz [b], José J. Ortega [c], Elisa Poveda [b], Jesús Mínguez [a], Rena Yu [b], Ángel De La Rosa [b], Miguel Á. Vicente [a]

[a] Department of Civil Engineering, University of Burgos, C/ Villadiego s/n, 09001 Burgos, Spain
[b] ETSI Caminos, C. y P, Universidad de Castilla-La Mancha, Av. Camilo José Cela s/n, 13071 Ciudad Real, Spain
[c] ETSI Minas y Energía, Universidad Politécnica de Madrid, C/ Alenza, 4, 28003 Madrid, Spain

ARTICLE INFO

Keywords:
Size effect in fatigue
Steel fiber–reinforced concrete
Computed tomography
Mesostructure

ABSTRACT

This study deals with the influence of the fiber concrete mesostructure on the size effect under compressive fatigue loading. For this purpose, three series of cylindrical specimens of steel fiber–reinforced concrete were fabricated. Before fatigue testing, all the cylinders were scanned and the main morphological, orientation, and distribution parameters of the pores and fibers were checked. The images reveal that, near the cylinders' walls, the porosity is lower than that in the cores and is even lower for large sizes. Additionally, larger specimens are more vulnerable to compressive fatigue loading, resulting in a reduction in fatigue life.

1. Introduction

Fatigue may affect the service life of concrete structures subjected to repetitive loads, such as railway slab tracks [1] or towers for wind turbines [2]. The addition of steel fibers can improve the capacity of concrete against fatigue [3], as they provide a distributed reinforcement in the concrete matrix. Fibers produce a bridging effect that can effectively control cracking by limiting the width of cracks and their propagation. Likewise, they provide significant resistance to bending and shear across developing cracks [4,5]. Therefore, steel-fiber reinforced concrete (SFRC) demonstrates a pseudo-ductile response, even in compression [6–8], increased residual strength (especially in tension), and enhanced energy dissipations capacities [9], relative to the brittle behavior of plain concrete mixtures. Fatigue tests to determine the response of fiber-reinforced concrete can be carried out under compressive [10], tensile [11], or flexural [12] loading conditions.

Regarding compressive fatigue, steel fibers reduce the material sensitivity to low frequencies —below 1 Hz— which is especially relevant for slender structures like towers for wind turbines [13,14]. Steel fibers increase the life of concrete under compressive fatigue, and there is an optimum fiber content —leading to the longest life— related to concrete mesostructure and fiber characteristics [15]. Similarly, fiber orientation and matrix porosity influence the concrete fatigue behavior as well [16–18]. In addition, unwanted stress gradients in compressive fatigue of SFRC significantly reduce the fatigue life [19], which suggests minimizing the loading eccentricity in compressive fatigue tests. Finally, experimental scatter in compressive fatigue results is large, so it is recommended to use a wide sample size [20], and to analyze the results with an appropriate statistical approach [14,21,22].

Size and shape of the tested specimens influence the concrete compressive strength [23,24]. Small specimens have higher strengths than larger ones. Following the same principle, a real-scale structure may exhibit an even smaller strength, thereby highlighting the importance of a correct assessment of its real value. The size effect has different causes. From a statistical point of view, the heterogeneity of concrete leads to a higher probability of larger specimens containing flaws that accelerate the failure of the material [25]. From a deterministic point of view, different mechanisms have been proposed. The explanation from the perspective of fracture mechanics is related to the different elastic energy stored in the deformed body of the specimen that is released in the propagation of a unit length of crack during the fracture process. While the former depends on the volume of the specimen, the latter is determined by the specific fracture energy of the concrete, which is a constant material property [23]. In compression, another influencing mechanism is the effect of lateral confinement near the loading surfaces produced by the friction developed owing to the transversal expansion of the material [26]. In short specimens, the resistance is enhanced because the proportion of material positively

* Corresponding author.
E-mail address: dgonzalez@ubu.es (D.C. González).

https://doi.org/10.1016/j.ijfatigue.2022.107353
Received 14 June 2022; Received in revised form 14 October 2022; Accepted 19 October 2022
Available online 25 October 2022

affected by the confinement is higher. Another aspect that needs to be highlighted is the boundary or wall effect, which is caused by the alteration of the material layer in contact with the wall of the mold or the formwork. This effect also induces variations in the results for different sizes [23] because the influence of that layer, with constant width, diminishes as the cross-sectional area increases.

The size effect on concrete has been the topic of much research throughout the decades [23–32], but most of the studies have focused on static loading conditions. With respect to fatigue under cyclic loads, research is relatively scarce, and most studies treat flexural fatigue [33–37]. The size effect on the compressive fatigue of concrete has not received much attention. In a recent work by Ortega et al. [38], this topic was addressed by testing cubic specimens, whereas Taher and Fawzy [39] studied compressive fatigue by means of prismatic specimens with the same cross-section and different heights. The geometry of the specimens used in the aforementioned studies is highlighted, as it also influences the obtained value of the compressive strength of concrete, as mentioned previously. In particular, the slenderness, which represents the relation between the height and the transverse dimension of the specimen, determines the extent of the zone free of hindered transversal strains. Cylindrical specimens used in the mechanical characterization of concrete usually have a slenderness value of 2, which is double that of cubes.

The present research aims to study the compressive fatigue in cylinders of different sizes but with a fixed slenderness value. This is an extension of the study in [38], which dealt with cubes. Herein, cylinders of three different heights (150, 200, and 300 mm) with diameters equal to half of the corresponding height were tested. The material used for the specimens was fiber-reinforced concrete owing to its relevance in applications under fatigue loads. The fatigue behavior is studied by focusing, first, on the probabilistic trend of the number of cycles to failure and, second, on the evolution of compressive strain during the loading process. Furthermore, given the different sources of size effect explained earlier, the investigation presented in this article also places special emphasis on the study of the internal structure of the material to verify the influence of defects and inhomogeneities on the results obtained for the specimens of different sizes. This addresses the statistical size effect and the influence of wall effects. Defects are considered in this study as pores in the concrete matrix. Another factor that may contribute to the heterogeneity of this type of concrete is the manner in which the fibers are distributed.

Regarding porosity, relevant papers have been published about its influence on the strength, stiffness, or fatigue response of concrete, among other parameters [16,17,40–42]. However, to date, few studies have investigated the effects of porosity on the size effect [43,44]. This is partly because it is a strongly random and non-controllable parameter, which makes it difficult to study. Despite this obstacle, many effective techniques are currently available to study the porosity of concrete, among which computed tomography (CT) is one of the most important.

CT is a non-destructive technique that is widely used to examine the microstructure of materials. This technology can create a three-dimensional image of a sample, in which each voxel has a gray level that is directly related to its density. Therefore, it is very useful when analyzing heterogeneous materials whose components have different densities. For concrete, CT is mainly used to analyze the distribution and orientation of fibers [18,45,46], as well as its porosity and crack patterns [16,47–49]. Some studies have applied CT to investigate the size effect in concrete [43,50–52]. Among them, the one by Różański et al. [43] stands out. In their study, micro-CT was used to analyze the porosity and pore size distribution in different sizes of samples of mortar and gypsum, which were then subjected to uniaxial compressive tests. However, for this case, the great potential of CT was not fully exploited, as it was only used to obtain the basic global parameters.

In the present study, the CT technique was applied to analyze the shape and size of pores in the concrete matrix and the orientation of fibers. The specimens were scanned before fatigue testing using a CT device and three-dimensional images were processed to obtain the different parameters of individual pores and fibers. Afterward, the results were analyzed and correlated with the size of the specimens and their corresponding fatigue behaviors.

The remainder of this paper is structured as follows. The material and experimental procedures are presented in Section 2. The results are described and discussed in Section 3, and finally, the conclusions are summarized in Section 4.

2. Experimental program

2.1. Materials

For this research, 75 specimens divided into three series (resulting in 25 specimens per series) were cast. All specimens were cylindrical, with three different sizes: 150 × 300 mm (diameter × height), 100 × 200 mm, and 75 × 150 mm. The series were identified with the letters L (large), M (medium), and S (small). In all cases, the ratio of the height to the diameter was 2 (Fig. 1).

The material used in this study is the same as that in [38]. It is a self-compacting concrete reinforced with steel fibers. The design target compressive strength was 30 MPa at 28 days of age (cubic specimens with a side of 100 mm) [53]. We followed the design methodology developed by De La Rosa et al. [54] and selected the following materials: type II Portland cement (CEM II/B-L 32.5 N), tap water, superplasticizer (MasterEase 5025, Master Builders), occluded air reducer (MasterCast 212, Master Builders), limestone powder (Betocarb, Omya Clariana), a rounded feldspathic fine-aggregate, and a siliceous crushed coarse-aggregate. The particle sizes of the limestone filler and the fine aggregate were measured by laser diffraction, obtaining an average particle size of 0.5 mm and 0.012 mm, respectively. The coarse aggregate was washed to eliminate the extra contribution of fines, and sieved to control its granulometry, obtaining a particle size range between 4 mm and 8 mm. The steel fibers used are straight, with 13 mm in length and 0.20 mm in diameter (Dramix OL 13/0.20, Bekaert), added in a content of 0.3%. Table 1 lists the quantities used.

Because of the necessary volume of concrete to be manufactured, a total of four batches were manufactured, following a rigorous control so that the manufacturing conditions were as similar as possible: humidity and environmental temperature control, initial drying of materials, manufacturing protocol, execution of tests in the fresh state, and placement in the concrete molds. The characterization of the behavior of the concrete in the fresh state was carried out using the slump flow test [55]. In no case were signs of segregation, bleeding, piling up of fibers,

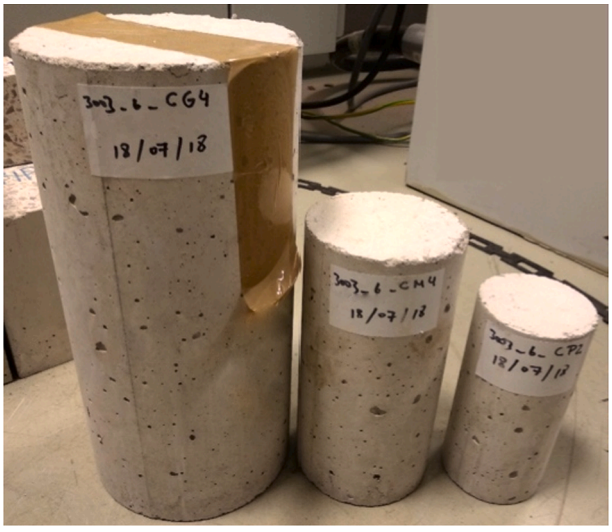

Fig. 1. Photograph of specimens belonging to series L, M, and S.

Table 1
Mix proportion of concrete.

Component	Content (kg/m^3)
Cement CEM II/B-L 32.5N	286
Water	202
Superplasticizer	2.86
Air reducer	1.00
Steel fiber	23.55
Limestone filler d50$^{(*)}$ = 12 μm	195
Feldspathic sand d50$^{(*)}$ = 0.5 mm	921
Crushed siliceous coarse aggregate d50$^{(*)}$ = 7.4 mm	712

$^{(*)}$ d50 is the average particle size.

or bubbling observed in the execution of these tests. After 24 h, the specimens were removed from the molds and placed in a climatic chamber, maintaining constant conditions of humidity (97% ± 0.3%) and temperature (20 °C ± 0.5 °C) until reaching the test age, which was of 19 months in the average. We also made three small cylinders for controlling the properties in the hardened fiber concrete, to ensure that scatter among batches was small. All the cylinders were stored in a humid chamber at 20°C and 96% relative humidity until the control tests when they were 10 months old. For these tests, we used a hydraulic machine brand Servosis, model MES-300. The loading rate was 0.3 MPa/s. The hinge of this machine is quite large and does not rotate during the tests. The control tests yielded the following average (and standard deviation) compressive strength for the four batches: 32.7 ± 1.0 MPa, 31.2 ± 0.4 MPa, 28.9 ± 0.3 MPa and 30.1 ± 1.6 MPa. The scatter for the strength of each batch is low and, likewise, taking all the results together as if they came from a single batch, we got strength of 30.7 ± 1.6 MPa, still with a low scatter. Therefore, the material throughout batches is considered homogeneous. Consequently, the cylinders for the monotonic and cyclic tests of each size were selected randomly among batches.

2.2. Testing procedure

Of the 25 specimens for each series, 10 were subjected to a monotonic compression test, following the European standard UNE-EN 12390–3 (2020) [56], to determine the average compressive strength of the concrete (f_{cm}) prior to the beginning of the fatigue tests (cylinders were 19 months old in average). For these monotonic tests we used self-designed individualized ball-and-socket joints, see Fig. 2, allowing rotation during the test to minimize loading eccentricity and its scatter. The actuator used was an MTS, model 201.7, with a load cell model 661,31F-01, and the loading rate of the monotonic tests was 0.5 MPa/s.

The remaining 15 specimens of each series were tested until failure under compressive fatigue loading at a frequency of 0.25 Hz, which is typical for wind turbines towers and facilitates fatigue testing for the big cylinders. Concrete fatigue life is usually shorter for frequencies below 1 Hz, but Medeiros et al. [13] showed that steel fibers prolong the life and restore the number of resisted cycles to those obtained with 1 Hz or higher. In all cases, the maximum and minimum stresses were 85% and 20%, respectively, of the average compressive strength of each size series, and we kept these values through the entire fatigue series since our objective was to study the effect of the size of the cylinder on the fatigue life and compare them with the results previously obtained in cubes of the same material with the same stress limits [38]. In these fatigue tests we also used the self-designed individualized ball-and-socket joints to minimize the effect of load eccentricity scatter during fatigue loading (see Fig. 2 for the cylinders prepared for fatigue testing) [19]. Three different ball-and-socket joints were used (one for each series), with their dimensions adapted to the corresponding specimen diameter. The spherical plain bearing increases the fatigue life and reduces the dispersion. The actuator and load cell were the same as in the monotonic tests to obtain the compressive strength. Typical broken specimens are shown in Fig. 3.

The strain–time curves were recorded for some specimens (14 specimens of series S, 9 specimens of series M, and 3 specimens of series L) throughout the test using three 50 mm long uniaxial strain gauges (1-LY41-50/120, HBK Naerum, Denmark). The strain gauges were glued in the longitudinal direction of the specimen, approximately at its center and 120° apart in the circumferential direction. Some of the gauges are visible in Figs. 2 and 3. The strain gauges were connected to an HBK QuantumX datalogger, which recorded the strain of the specimen throughout the fatigue test, as well as the load value applied at each point in time. The recording rate was 5 Hz.

2.3. CT scanning and image post-processing

Seven specimens each from series S and M were scanned using a GE Phoenix v|tome|x (General Electric, Boston, MA, USA) device before starting the fatigue test. The CT scan device was equipped with an X-ray tube of 300 kV/500 W, including software that provides sectional images of the specimens with a resolution of 2048 × 2048 pixels. The pixel size and spacing between consecutive slices were both 35 μm, so the voxel size (volumetric pixel) was 35 × 35 × 35 μm^3. Note that this resolution is optimum for studying the mesoscale of the material but does not allow for resolving the microscale. Owing to the limitations of the CT scan device, it was unable to scan specimens from the L series.

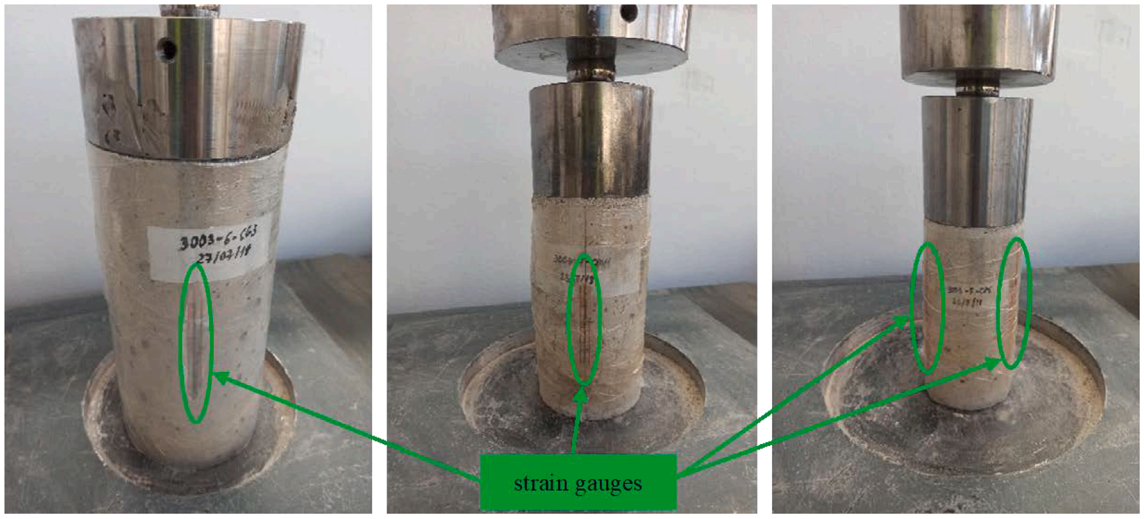

Fig. 2. Cylinders L, M, and S (left to right) with their individualized ball-and-socket joints prepared for the fatigue test.

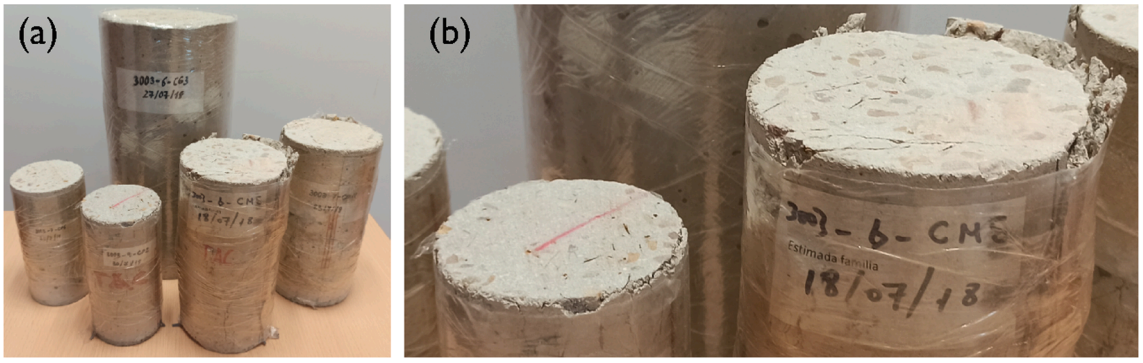

Fig. 3. (a) Some broken specimens belonging to series M and S. The picture also shows an intact L cylinder for size comparison. (b) Zoom of the bases of the foreground S and L broken cylinders.

The software included in the CT scan works with 16-bit images, so a gray value in a range varying from 0 to 65,535 is assigned to each voxel, where 0 denotes black and 65,535 means white. The value assigned depends on the linear attenuation coefficient μ of the material, which in turn depends on the density. Therefore, light gray voxels (high values) belong to more dense points (i.e., steel fibers), while dark gray voxels (low values) belong to less dense points (i.e., pores). The outcome of the scanning process is a matrix including the X, Y, and Z coordinates of the center of gravity of each voxel, and its gray value is obtained. More detailed information regarding CT can be found in [57–60].

Image post-processing was performed using the digital image processing (DIP) software AVIZO (FEI Visualization Sciences Group, Hillsboro, OR, USA). This tool enables the identification and isolation of individual pores and individual fibers in the specimens. First, the software identifies the voxels belonging to pores, which are those whose gray value is under an inferior threshold value, and belonging to fiber, which are those whose gray value is above a superior threshold value. The histograms of the gray distribution of all specimens were analyzed with the aim of selecting a suitable threshold value.

Subsequently, the DIP software merges the voxels in contact belonging to pores, creating groups that correspond to the pores in the concrete specimens. Similarly, this software merges the voxels in contact belonging to fibers. Figs. 4 and 5 show the pores and fibers identified and isolated in one specimen of each series. Finally, the data of each pore can be obtained: X, Y, and Z coordinates of the center of gravity, as well as its volume, surface, length, etc. The length of a pore is defined as the maximum distance between two voxels belonging to the same pore. In this study, only pores equal to or greater than 0.1 mm, that is, with more than 3 voxels in their largest direction, were considered. The remaining ones were discarded because their parameters could not be determined with sufficient accuracy. Regarding the fibers, only the orientation of each fiber was extracted.

The results show the average values of the seven specimens of each series (see Subsection 3.3). In all cases, the variability between samples belonging to the same series was relatively low.

3. Results and discussion

By analyzing the information from the static and fatigue tests as well as from the CT scan device, useful data that can aid in understanding the correlation between the mesostructure of the concrete and its macroscopic response can be obtained.

Table 2 presents the mean compressive strength results for each size, as well as their standard deviations. These mean values serve as a reference to determine the minimum and maximum stress of the loading cycles.

Note that the average compressive strength of the reference S cylinders is smaller than the average compressive strength of the control S cylinders. This strength difference may be due to a different maturation process of the two sets of specimens, a dissimilar testing process, or both.

Curing conditions only could have favored that the reference S cylinders yielded higher strengths due to the 9 additional months in a

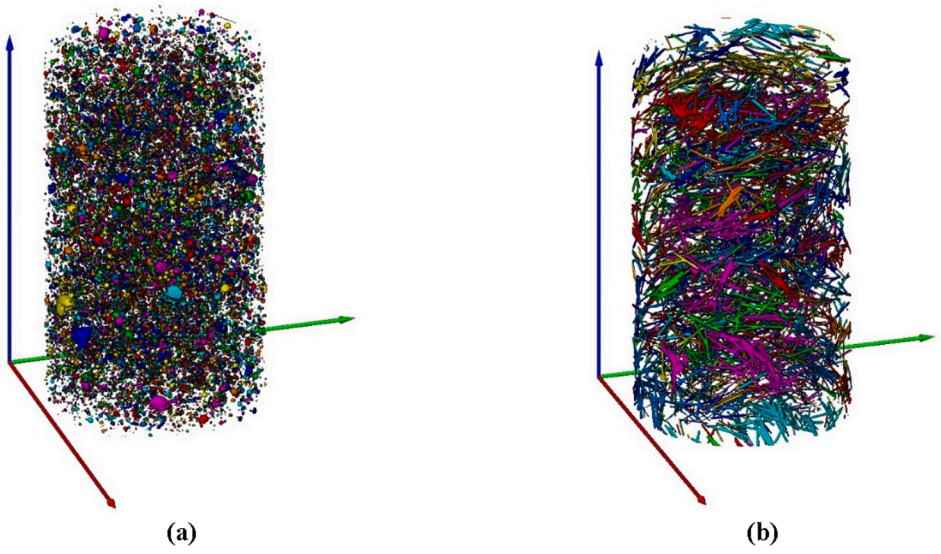

Fig. 4. Post-processing of CT images of an S series specimen and discretization of the components of interest: (a) pores and (b) fibers.

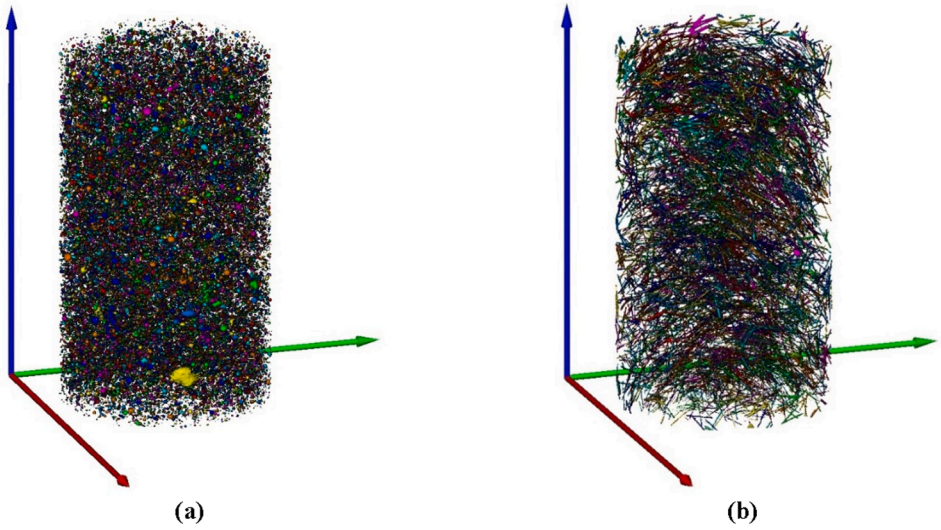

Fig. 5. Post-processing of CT images of an M series specimen and discretization of the components of interest: (a) pores and (b) fibers.

Table 2
Compressive strength of specimens.

Specimen	f_c (MPa)	Specimen	f_c (MPa)	Specimen	f_c (MPa)
S-16	27.9	M-16	33.1	L-16	33.4
S-17	21.3	M-17	24.5	L-17	33.2
S-18	29.4	M-18	32.1	L-18	31.9
S-19	26.7	M-19	26.6	L-19	32.0
S-20	24.3	M-20	29.5	L-20	32.5
S-21	22.3	M-21	31.3	L-21	32.8
S-22	30.0	M-22	29.3	L-22	31.7
S-23	31.5	M-23	27.1	L-23	32.4
S-24	23.6	M-24	30.0	L-24	32.8
S-25	26.5	M-25	26.2	L-25	32.0
Average	26.3	Average	29.0	Average	32.5
Std. Dev.	3.4	Std. Dev.	2.8	Std. Dev.	0.6

humid chamber. The difference in the loading rates is not high, but it also would have worked in the same direction. However, the boundary conditions of the reference tests led to getting lower strengths. We attribute this fact to using the individualized ball and socket joint along with the material being heterogeneous in cylinders due to the wall effect, which will be studied deeply in Section 3.4. Fig. 3b is a zoom of the top of the L and S tested cylinders in Fig. 3 of the paper. It shows that the crack patterns of the broken cylinders tend to form a conical crack at the top that penetrates inside the specimen and generates spalling of the cylindrical surfaces. In some cases, these walls protrude from the top base since the upper platen has the same diameter as the cylinder (see Fig. 3b). This hints that the material forming the tube around the specimen due to the wall effect resists more than the material inside the cylinder. This can explain that control tests, in which the platen impedes the tube wall to protrude and forces it to break along with the inner material, give more strength than the ones done with the individualized ball-and-socket joint.

3.1. Static tests

It is noteworthy that the average compressive strength increases by 24% when the cylinder diameter increases twofold (from 75 mm for series S to 150 mm for series L), which cannot be attributed to experimental scatter since we tested ten cubes for each size, the standard deviation is small, and the coefficient of variation is 13%, 10% and 2% for the S, M and L series, respectively. This strength increase is contrary to the well-known size effect, which would have predicted that the smaller specimen would be stronger. To gain insight into this interesting phenomenon, we examined the mesostructure using the CT images, and the results are presented in Section 4.

3.2. Fatigue tests

Table 3 lists the fatigue life of each specimen.

To compare the results obtained from the different series, a Weibull fitting [16–18] was performed on the fatigue data of Table 3. The results are depicted in Fig. 6, which reflects the probability of failure versus the logarithm of the number of cycles, *N*, obtained experimentally. In addition, for each series, we drew the curve fit corresponding to the two-parameter Weibull distribution. Moreover, we presented the results obtained in [38] on cubes of 40, 80, and 150 mm at the edge.

The Weibull distribution, commonly used to model fatigue life, is based on the weakest link hypothesis [25]. This means that an element fails when its weakest point fails, assuming that the material is composed of small units connected in series. This approach seems reasonable for small and not very complex structural elements (e.g., linear elements under tension) but not for more complex structural elements where there may be different "critical paths" of failure.

Le, Bažant, and Bažant [61] proposed a different approach for larger and more complex structural members, where different failure

Table 3
Fatigue life of each specimen.

Specimen	N	Specimen	N	Specimen	N
S-01	416	M-01	27	L-01	828
S-02	6270	M-02	17	L-02	140
S-03	22,429	M-03	242	L-03	212
S-04	213	M-04	20	L-04	13
S-05	922	M-05	16	L-05	6
S-06	5675	M-06	1511	L-06	5
S-07	7674	M-07	6	L-07	89
S-08	4128	M-08	741	L-08	1953
S-09	138	M-09	238	L-09	96
S-10	3082	M-10	36	L-10	310
S-11	22,259	M-11	238	L-11	407
S-12	514	M-12	40	L-12	172
S-13	3892	M-13	297	L-13	4
S-14	2940	M-14	6	L-14	2
S-15	1499	M-15	15	L-15	1612
Average	5470	Average	230	Average	390
Std. Dev.	7241	Std. Dev.	406	Std. Dev.	609

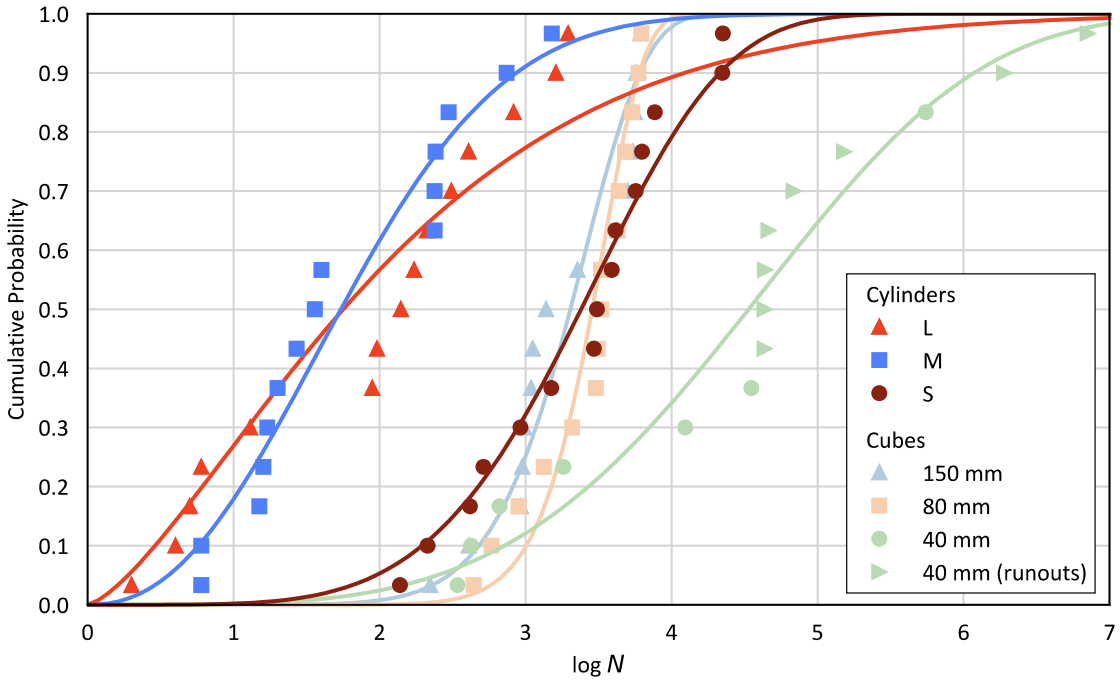

Fig. 6. Weibull fitting of fatigue life in all series of cylinders in this research compared with the three series of cubes in [38]. All specimens were made of the same material and all fatigue tests were run from 20% to 85% of the compressive strength of the corresponding series.

mechanisms exist, and which are interrelated by series and parallel connections.

Fig. 6 shows that both series L and M exhibit similar behaviors. In contrast, the S series indicates a curve noticeably shifted to the right, which means that its fatigue life is clearly longer than those of the L and M series. As the x-axis is plotted in logarithmic scale, this difference is approximately two orders of magnitude. The behavior is analogous to that observed by Ortega et al. [38]. However, cylinders endure fewer cycles than cubes of the corresponding size. For instance, the log *N* at 50% probability of failure for the large/medium cylinders is roughly 1.7, while for large/medium cubes is roughly 3.4. So, for these sizes, the shift in the *x*-axis is approximately two orders of magnitude. Small specimens behave differently since the shift is only of roughly one order of magnitude between cylinders and cubes for a 50% probability of failure. It should be emphasized that all cylinder and cube specimens in Fig. 6 had the same material and all tests were run from 20% to 85% of the compressive strength of the corresponding series. The results show that the specimen size substantially influences the fatigue life. Likewise, the shape of the specimen considerably affects the fatigue behavior, with cylinders being more conservative than cubes.

The Weibull fitting curve has the following mathematical expression (eq. (1)):

$$F(\log(N)) = 1 - e^{-\left(\frac{\log(N)}{\lambda}\right)^{\beta}} \quad (1)$$

Here, β and λ are the shape and scale coefficients, respectively. The values of these coefficients for the different series are listed in Table 4.

The coefficient β is related to the sharpness of the curve and, consequently, to the dispersion of the results. In particular, the higher the coefficient β, the steeper the curve, and therefore, the less the data scattering. The L series shows the highest dispersion of the results, whereas the S series has the lowest variation.

Table 4
Coefficients β and λ of the Weibull fitting, with their corresponding goodness coefficient (R^2).

Series	β	λ	R^2
L	1.42	2.27	0.94
M	2.28	2.04	0.94
S	4.85	3.65	0.98

The coefficient λ is related to the position of the curve along the abscissa, that is, the fatigue life. The higher the coefficient λ, the farther the curve location to the right, and therefore, the longer the fatigue life. Series S shows a significantly higher λ value than the other two series, which have very similar values. This means that the fatigue lives of series L and M are very similar, while that of series S is clearly higher. The results indicate that the specimen size substantially influences the fatigue life of the element.

From the information provided by the strain gauges, the fatigue creep curve of each specimen, which represents the evolution of the maximum strain with the cycles, was obtained (Fig. 7). The strain corresponds to the average value of the strain measured by each of the three uniaxial strain gauges arranged on the specimen.

All curves have the same trends. Initially, they show a significant increase in deformation (primary strain). Then, the strains of the specimens display a linear behavior with the cycles (secondary strain) up to a point where the strains increase very rapidly until rupture (tertiary strain).

The slope of the fatigue creep curve in its central zone is the secondary strain rate per cycle. This is a very interesting parameter because, according to Sparks and Menzies [62], it is directly related to the fatigue life. According to numerous published works [13,15,63], this parameter depends only on the concrete matrix.

Table 5 lists the secondary strain rates for each specimen measured in the second stretch of the strain-number of cycles curve, roughly between 20% and 80% of the fatigue life. As said before, in this study, not all specimens from the three series were instrumented; the strain–time curves were recorded on 14 specimens of series S, 9 specimens of series M, and 3 specimens of series L.

Fig. 8 illustrates the correlation between the secondary strain rate and fatigue life for each series.

As exhibited in Fig. 8, the secondary strain rate is strongly affected by the specimen size. For the S series specimens, the increase in

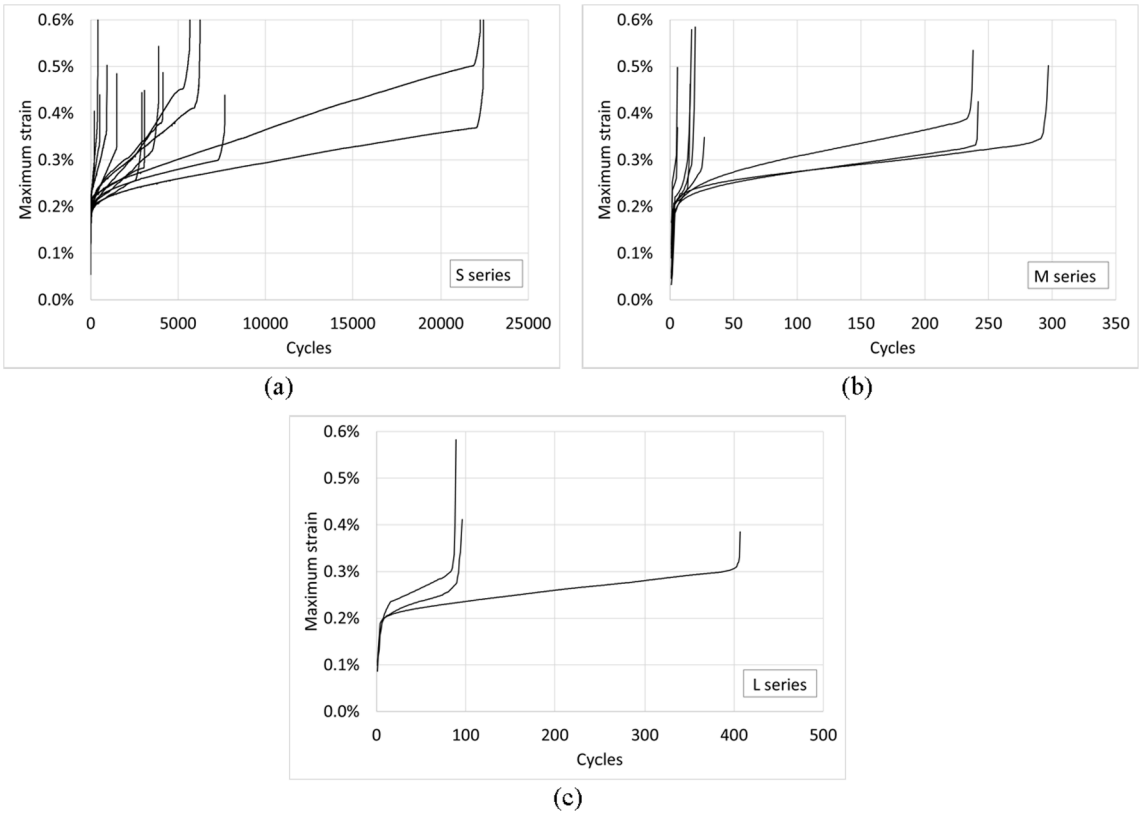

Fig. 7. Fatigue creep curves: (a) S series, (b) M series, and (c) L series.

Table 5
Secondary strain rate in specimens of each series.

Specimen	dε/dN	Specimen	dε/dN	Specimen	dε/dN
S-01	4.40E-06	M-01	3.26E-05	L-07	9.10E-06
S-02	3.14E-07	M-02	7.26E-05	L-09	5.93E-06
S-03	7.03E-08	M-03	4.06E-06	L-11	2.23E-06
S-04	2.69E-06	M-04	6.38E-05		
S-05	1.47E-06	M-05	2.84E-05		
S-06	4.52E-07	M-07	1.92E-04		
S-07	1.08E-07	M-11	6.01E-06		
S-08	4.56E-07	M-13	3.33E-06		
S-10	2.08E-07	M-14	8.80E-05		
S-11	1.21E-07				
S-12	2.44E-06				
S-13	3.30E-07				
S-14	2.45E-07				
S-15	8.58E-07				

deformation that occurs at each loading cycle ($d\varepsilon/dN$) is small, whereas for the M and L series specimens, this value is clearly higher. It can also be observed that all points in the graph are aligned along the same straight line, regardless of the series. The S series indicates smaller values of the secondary strain rate and longer fatigue life, so they are in the lower right part of the graph. In contrast, the M and L series display a larger value of secondary strain rate and a shorter fatigue life, so they are located in the upper right part of the graph. The correlation obtained is good, given that the line of fit presents a value of $R^2 = 0.968$.

It is evident that the relationship between the secondary strain rate and fatigue life is not affected by the size effect. Therefore, it is an intrinsic material relationship. This result agrees with that obtained by Ortega et al. [38] for cubic specimens. Other studies have also shown that this relationship does not depend on either the test frequency or fiber content in the case of fiber-reinforced concretes [14,15,64].

A phenomenon observed by Ortega et al. [38] for cubic specimens was the development of the maturation of the concrete, and its corresponding strengthening, thanks to the compressive fatigue loading. This autogenous self-healing due to fatigue loading can be explained by the new hydration reactions of cement particles when pore water moves through the network of microcracks that fatigue loading creates. This was confirmed by the reduction of pore volume in the range of 0.01–0.1 μm, which is analogous to the densification due to maturation in the same concrete kept in a humid chamber, which also showed strengthening. In the current experimental campaign over cylinders made of the same concrete that in [38], no further analyses were performed to verify the existence of fatigue maturation. Nevertheless, it is logical to assume that this phenomenon may also contribute to extend the life of small cylinders, as this fatigue maturation seemed to have more effect in smaller specimens in the case of the cubes.

3.3. Study of the mesostructure

Among the information that can be obtained from the CT scan, only that which is relevant to this study is presented for both the fibers and pores. In particular, using the data of the pores, the following information was extracted: the cumulative pore volume curves and porosity curves, sphericity and shape factors, and pore orientations. In addition, the fiber orientations were investigated. Note that the resolution of the CT scanner used in this research does not allow for observing the microstructure of the material.

3.3.1. Cumulative pore volume and porosity curves

Two different types of curves are commonly used to analyze the pore size distribution. First is the cumulative pore volume curve, which relates the length of each pore to the relative pore volume up to that length. Thus, the relative pore volume, defined as the ratio between the volume of pores considered (V_p) and the total volume of pores of the specimen ($V_{p,tot}$), is displayed on the ordinate (eq. (2)).

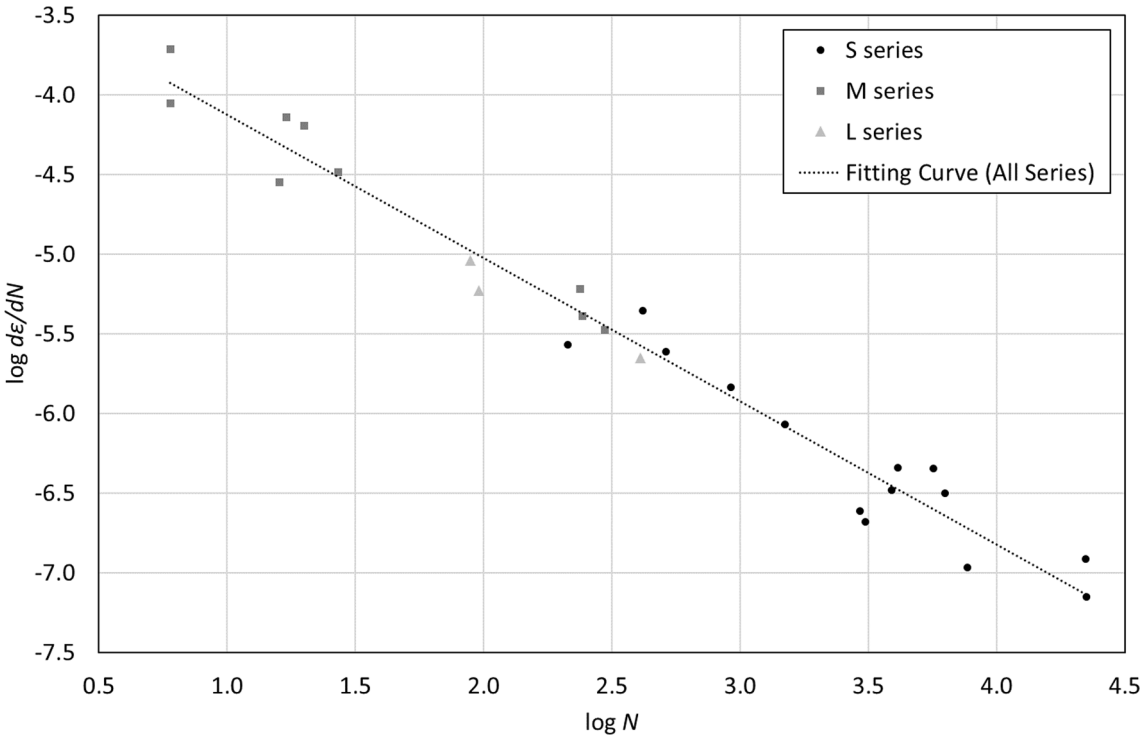

Fig. 8. Correlation between the secondary strain rate and fatigue life.

$$V_{p,rel} = \frac{V_p}{V_{p,tot}} \quad (2)$$

Second is the porosity curve, which relates the length of each pore to the porosity up to that length. Therefore, the porosity, which is the ratio between the volume of pores considered (V_p) and the volume of the specimen (V_s), is displayed on the ordinate (eq. (3)).

$$p = \frac{V_p}{V_s} \quad (3)$$

Figs. 9 and 10 illustrate the cumulative pore volume and porosity curves, respectively. Both series S and M are plotted on the graphs.

The cumulative pore volume curves reveal that both series have slightly different behaviors. The curves of the S series are slightly more inclined than those of the M series. This indicates that the M series

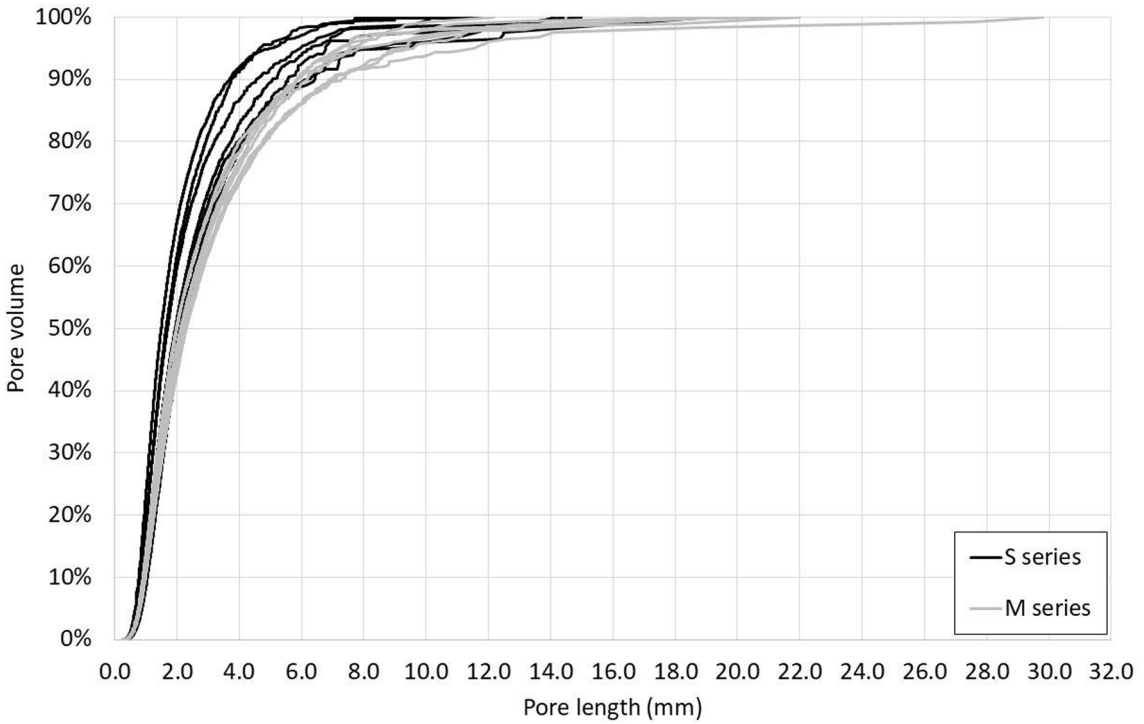

Fig. 9. Cumulative pore volume curves of series S and M.

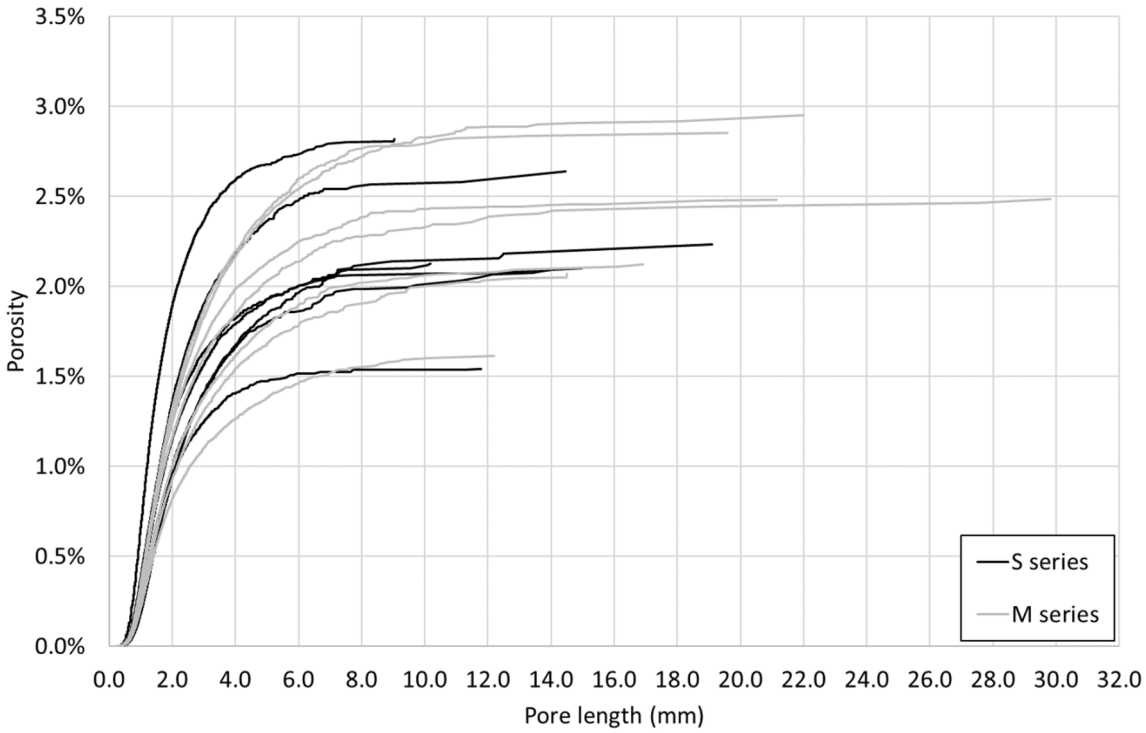

Fig. 10. Porosity curves of series S and M.

specimens have larger pores. This result is corroborated by the porosity curves (Fig. 10), where it can be seen that the curves of all specimens are similar and no trend can be observed, except that, in general, the curves of the M series specimens are located further to the right. This means that the M series specimens have larger pores.

From the cumulative pore size curves, the "maximum pore size" ($T_{max,pore}$), which is defined as the length at which 90% of the total pore volume is less than or equal to it, can be obtained. Additionally, one can define the characteristic porosity (p_{ch}), which is the total relative volume of pores whose length is less than or equal to the maximum pore size [60,65]. Table 6 provides the results for both parameters. The values in brackets correspond to standard deviations.

The table shows results in accordance with the results described above. The maximum pore size of the S series specimens is lower than that of the M series. On the other hand, the characteristic porosity is practically identical in both cases.

Both series show very similar porosity, being the difference in the pore size distribution. The S series has smaller pore sizes, while the M series has larger pores. Therefore, the size of the specimen determines the maximum pore size that can be accommodated.

This is apparently a size effect of a statistical nature, such that the larger the specimen, the greater the probability of hosting a larger number of larger pores. However, it is important to highlight it, because this effect causes, de facto, a variation in the mesostructure of the concrete that has consequences on the mechanical response, as shown below.

For each of the specimens of both series, it is possible to obtain their $T_{max,pore}$ and fatigue life. Fig. 11 shows the correlation between both parameters.

Based on Fig. 11, there is a clear correlation between the maximum pore size and fatigue life, such that the larger the $T_{max,pore}$, the shorter the fatigue life. The correlation is strong, given that the line of fit has a value of $R^2 = 0.809$. The results indicate that larger pores influence the fatigue response. Microcracking under compressive fatigue loading starts mainly in the larger pores, which are the most vulnerable. The M series specimens, which have larger pores (reflected by their higher $T_{max,pore}$ values), are more vulnerable to compressive fatigue and have a shorter fatigue life. In contrast, the S series specimens, which have smaller pores, are less vulnerable to compressive cycles and have a longer fatigue life.

Note that large pores are also more vulnerable to monotonic loading. Thus, we should not have obtained an inverse but a regular size effect on the compressive strength of the cylinders, which corresponds to the initial distribution, for N = 1, following the expression by Saucedo et al. [14]. A plausible justification for this abnormal behavior can be obtained from the analysis of the wall effect, which is presented below. Additionally, it should be noted that the inverse size effect in monotonic loading may occur after the longer life of the S series cylinders because their absolute cyclic stress levels are lower than those of the M and L specimens.

A comparison of the results obtained by Ortega et al. [38] regarding fatigue maturation with those found in this study (in particular, the results indicated in Fig. 6) reveals that compressive fatigue loading generates opposite effects acting on different scales. Cyclic loading in compression causes the formation and growth of cracks, which progress and aggregate until the specimen collapses. These cracks arise mainly in larger pores and thus influence the fatigue life. Furthermore, compressive fatigue loading produces progressive densification of the matrix on a micrometric scale. This phenomenon seems dominant in small specimens, at least in cubes [38] and likely in cylinders, and thus influences the observed size effect on fatigue.

Table 6
Maximum pore size and characteristic porosity for series S and M.

Parameter	S series	M series
$T_{max,pore}$ (mm)	5.1 [1.1]	6.4 [0.6]
p_{ch} (mm^3/mm^3)	0.020 [0.004]	0.021 [0.004]

3.3.2. Sphericity and shape factors

The sphericity and shape coefficients of the specimens were determined. The sphericity coefficient is defined as the quotient between the volume of the pore and the product of its outer area by its length, while the shape coefficient is the quotient between the volume of the pore and

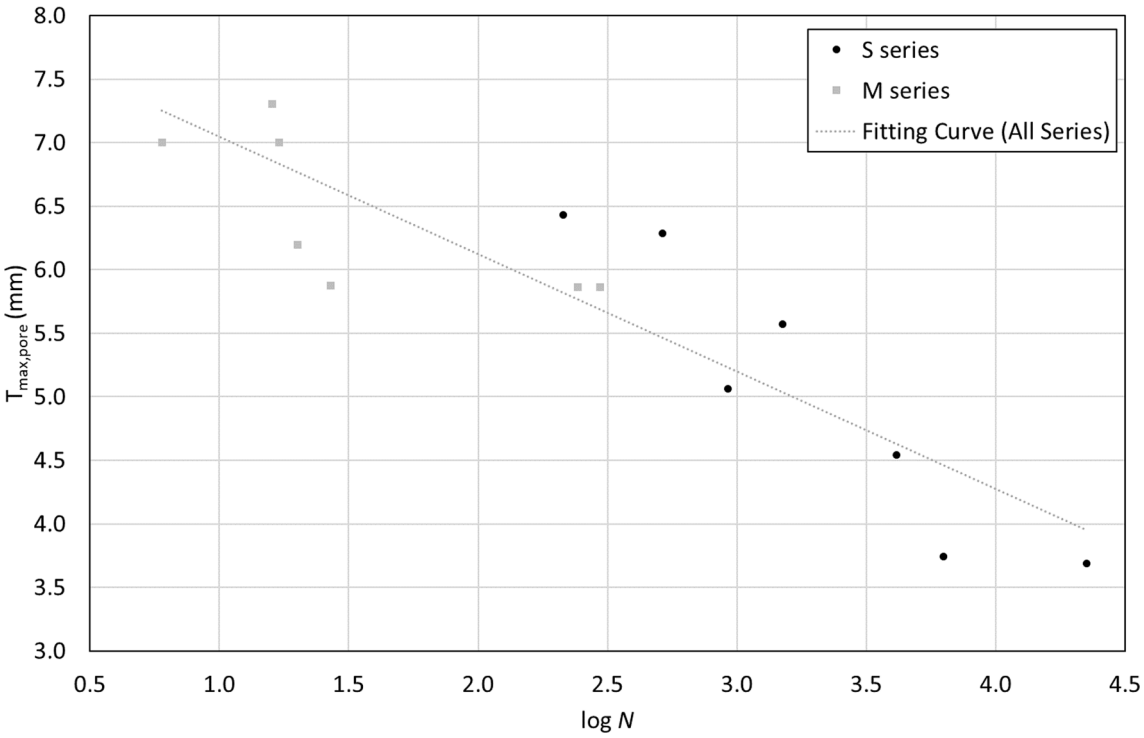

Fig. 11. Correlation between maximum pore size and fatigue life for series S and M.

the volume of the circumscribed sphere [60].

Figs. 12 and 13 show a comparison of the values of the sphericity and shape factors, respectively, for series S and M.

The results show that, in general, the pores tend to be elongated and not rounded, as might be expected a priori. As for the sphericity coefficient, the most frequent value is between 0.125 and 0.130, that is, between 75% and 78% of the value corresponding to a perfect sphere (which is 0.167).

The shape coefficient exhibits a behavior similar to that of the sphericity coefficient. The pores have an elongated shape. The most frequent value is between 0.350 and 0.375, that is, between 35% and 37.5% of the value corresponding to a perfect sphere.

Table 7 lists the positions of the center of gravity of the sphericity coefficient and the shape coefficient for each series. The values in

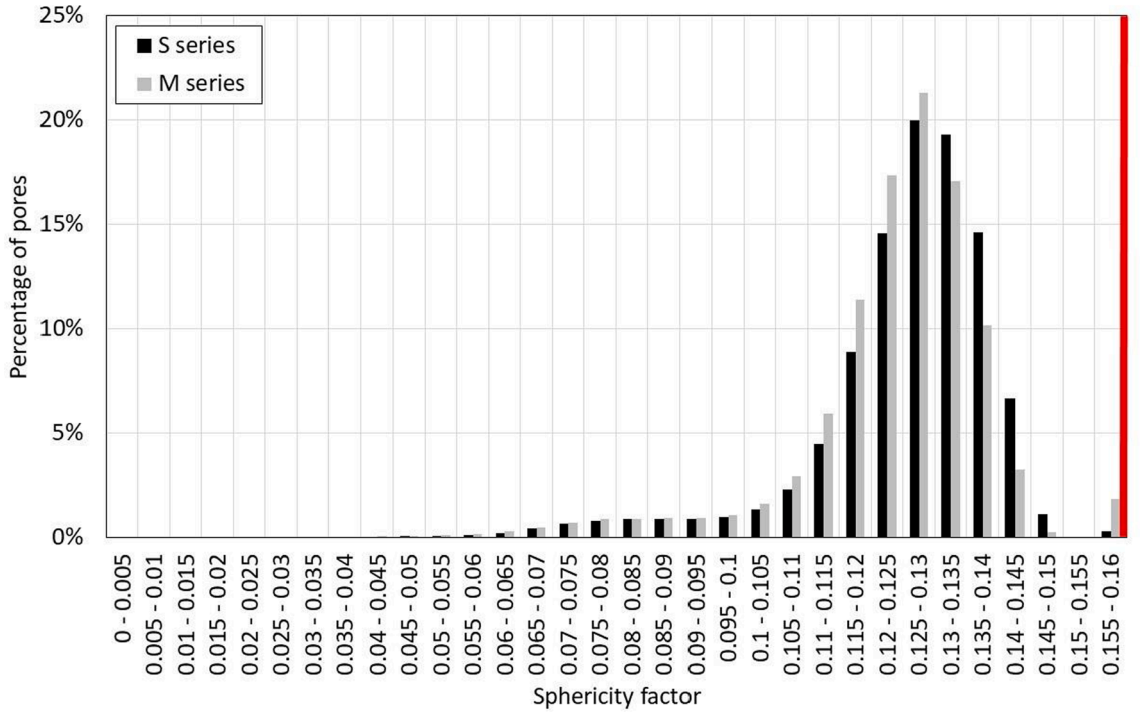

Fig. 12. Comparison between the average values for sphericity factors of series S and M. Note that the sphericity factor of a sphere is 0.167 (red vertical line in the plot). (For interpretation of the references to colour in this figure legend, the reader is referred to the web version of this article.)

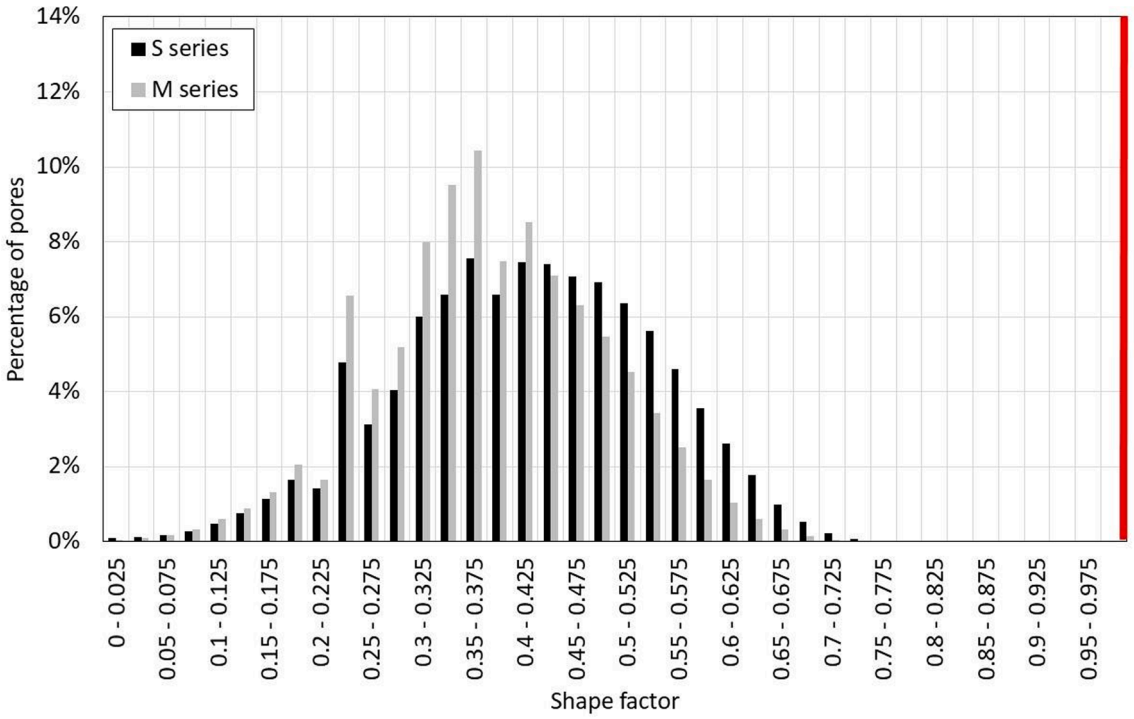

Fig. 13. Comparison between the average values for shape factors of series S and M. Note that the shape factor of a sphere is 1.000 (red vertical line in the plot). (For interpretation of the references to colour in this figure legend, the reader is referred to the web version of this article.)

Table 7
Mean values and standard deviations of the sphericity and shape factors for series S and M.

Series	Sphericity factor	Shape factor
S	0.127 [0.002]	0.427 [0.026]
M	0.124 [0.002]	0.390 [0.013]

brackets correspond to standard deviations.

Both the shape coefficient and sphericity coefficient reveal that the two series have very similar behaviors. However, series S shows slightly larger values, indicating that its pores tend to be slightly more rounded. This is consistent with the results depicted in the previous figures, because the smaller pores tend to be more rounded, while the larger pores tend to have more irregular shapes, as they adapt to the gap between the solid components of the cementitious matrix. Series S has a higher percentage of small pores, whereas series M has slightly larger pores.

Comparing the data presented in Table 7, it is evident that the S series specimens have smaller and less elongated pores, while those of the M series have slightly larger and less rounded pores. However, because the difference between the specimens is small, correlations between the pore shape and other morphological and/or response parameters under fatigue loading cannot be observed.

3.3.3. Fiber orientations

The fiber orientations were determined. In this study, given the cylindrical geometry of the specimens, their orientations were perfectly defined using two angles (Fig. 14):

1. Gamma angle (γ), which is the angle formed by the fiber with the vertical axis. In other words, γ is the angle that the fiber makes with the load axis during the test. This is an important angle when the load is applied along this axis.
2. Radial angle (ρ), which is the angle between the horizontal projection of the fiber and the radial axis. The radial axis is defined as the axis joining the center of gravity of the fiber with the center of the cross-section.

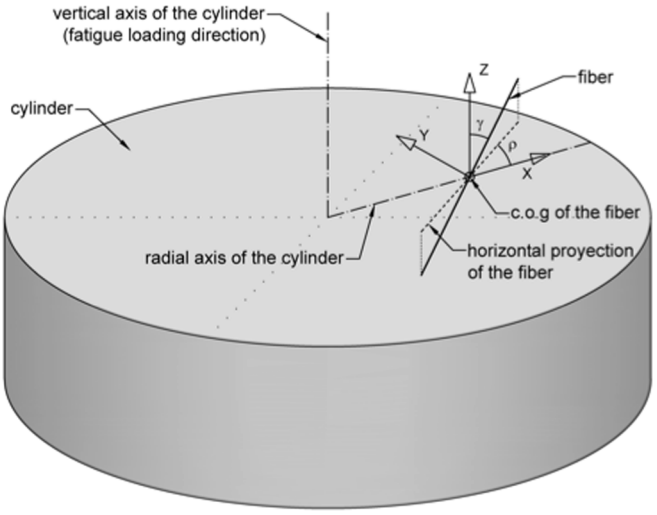

Fig. 14. Definition of angle γ and radial angle ρ. Here, the X-axis is the radial axis, whereas the Z-axis is the loading direction.

Alternatively, the circumferential angle, which is complementary to the radial angle, can be defined.

Figs. 15 and 16 display the histograms of the fiber orientation distributions for series S and M, according to both the gamma and radial angles, respectively.

Based on the information from the figures, it is possible to determine the efficiency indices, which are defined according to the following expressions [60,66] (eqs. (4) and (5)):

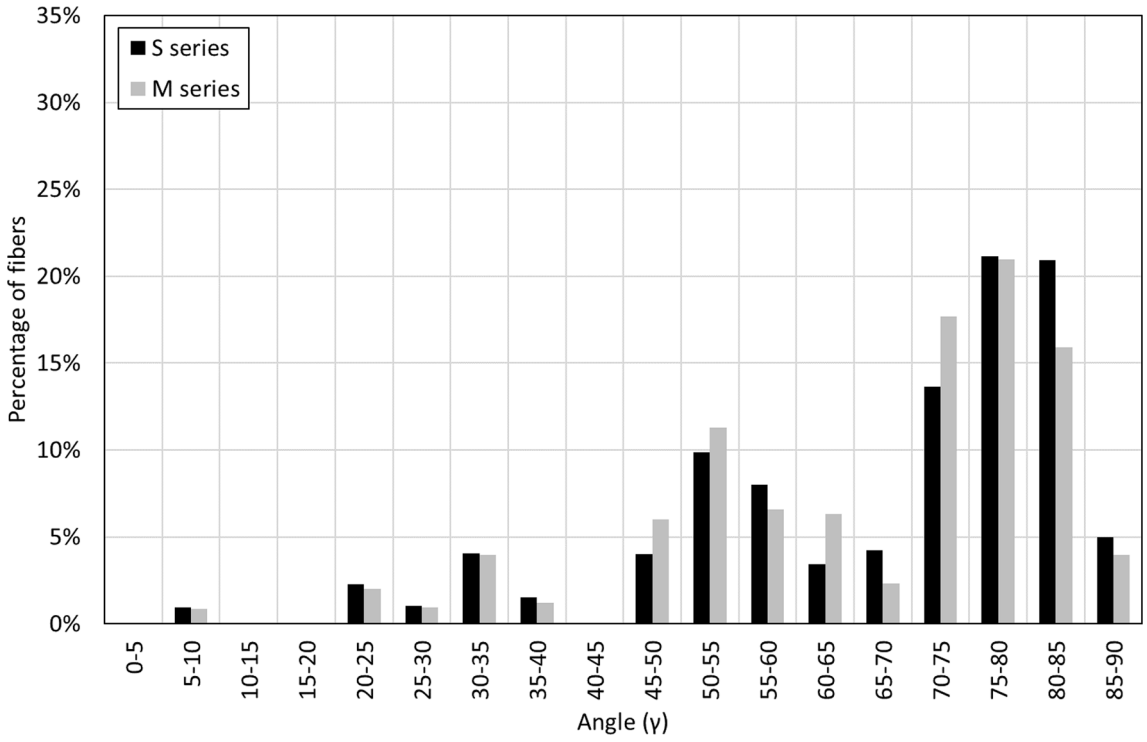

Fig. 15. Comparison of histograms of average fiber orientations according to angle γ for series S and M.

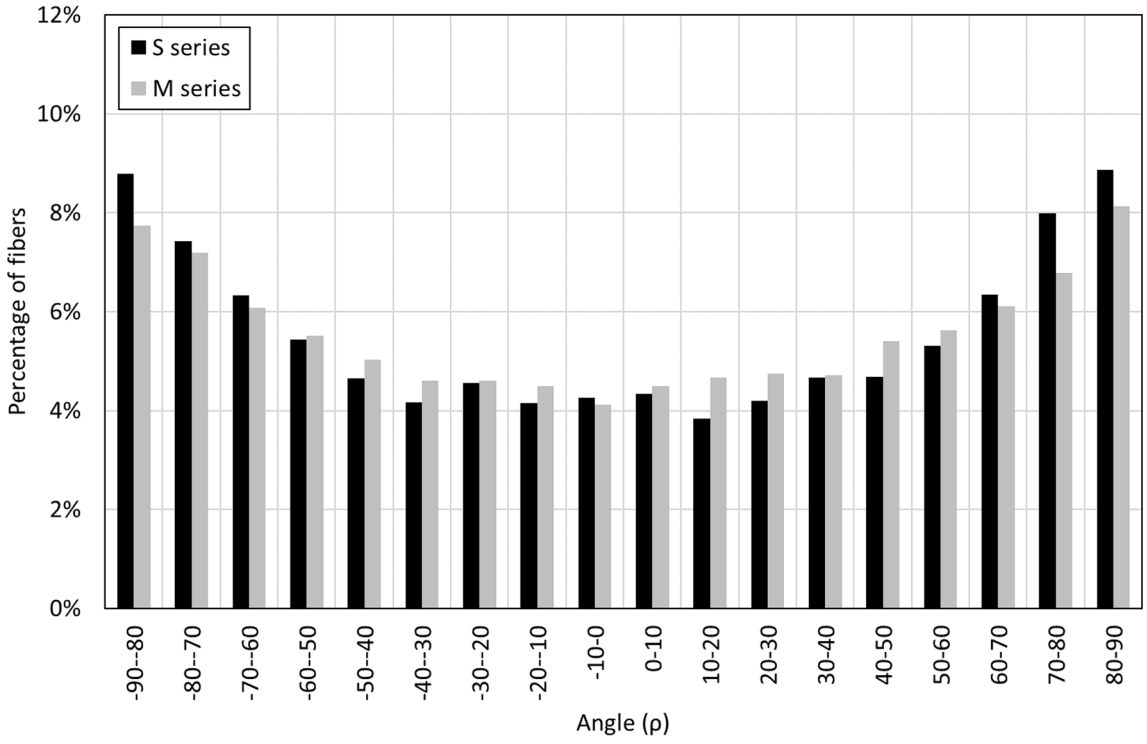

Fig. 16. Comparison of histograms of average fiber orientations according to radial angle ρ for series S and M.

$$e_\gamma = \sum_{i=0}^{n} f_i \cos^2 \overline{\gamma_i} \tag{4}$$

$$e_\rho = \sum_{i=0}^{n} f_i \cos^2 \overline{\rho_i} \tag{5}$$

where $\overline{\gamma_i}$ and $\overline{\rho_i}$ are the average values of each angular range, f_i is the frequency related to each angular range, and n is the number of ranges of the histogram.

The efficiency index takes values between 0 and 1, where 1 denotes that the fibers are perfectly oriented with the reference axis while 0 means that the fibers are arranged perpendicular to it. Table 8 presents the results of this study. The values in brackets correspond to the standard deviations.

Table 8
Efficiency indices of fiber orientation according to the gamma and radial angles for series S and M.

Efficiency index	S series	M series
e_γ	0.19 [0.02]	0.20 [0.04]
e_ρ	0.41 [0.02]	0.43 [0.02]

Fig. 15 indicates that most of the fibers form an angle close to 90° with the vertical axis, that is, the fibers are oriented substantially along the horizontal plane. In addition, the efficiency index e_γ exhibits a small value. For both series, the efficiency index e_γ is very similar, which means that there is no difference between the two sizes. Similarly, Fig. 16 shows that most of the fibers tend to form an angle close to 90°. Consequently, the efficiency index e_ρ is less than 0.5. This behavior is observed in both series, although it is slightly more pronounced in the S series.

The fiber orientation is partially influenced by the wall effect, such that the fibers closer to the edge tend to be oriented parallel to it (i.e., in a circumferential direction). In the interior of the specimen, the fibers tend to be oriented randomly. In this study, the size of the region affected by the edge effect does not depend on the diameter of the specimen but on the length of the fiber. For the S series specimens, the edge effect influences a higher percentage of the cross-section and, thus, a higher percentage of the fibers. However, for the M series specimens, the edge effect is smaller.

3.3.4. Pore orientations

We compared the pore orientations of the different series of specimens. Because the pores, as mentioned in the previous sections, are not perfectly spherical, a main direction can be established.

As had been done for the fiber orientation, the pore orientation was perfectly defined using two angles:

1. Gamma angle (γ), which is the angle that the pore forms with the vertical axis, that is, with the load axis during the test. It is an important angle when the load is applied along this axis.
2. Radial angle (ρ), which is the angle that the horizontal projection of the pore creates with the radial axis. The radial axis is defined as the axis joining the center of gravity of the pore with the center of the section.

Figs. 17 and 18 illustrate the histograms of the pore orientation distribution for series S and M, according to both the gamma and radial angles, respectively.

Table 9 lists the efficiency indices of the different specimens according to the two angles studied. The values in brackets correspond to the standard deviations.

Fig. 17 indicates that most of the pores form an angle between 70° and 90° with the vertical axis, , the pores are oriented sensibly along the horizontal plane. In addition, the efficiency index e_γ shows a low value. The fundamental difference between the two series is that the S series shows that there are some pores with an orientation between 20° and 40° with respect to the vertical axis, which are not visible in the M series.

This means that the value of eγ for the S series is somewhat higher than for the M series.

On the other hand, Fig. 18 shows how the relative frequency increases as we move away from the 0° value, both to the right and to the left. Consequently, the efficiency index e_ρ is clearly lower than 0.5. This behavior is observed in both series, although it is slightly more pronounced in the S series.

Analogous to the fibers, the orientation of the pores is conditioned by the wall effect, so that the pores closest to the edge tend to orient themselves in a circumferential direction, i.e. parallel to the edge.

In the interior of the specimen, the pores tend to orient themselves randomly. The size of the annulus affected by the edge effect, for this purpose, does not depend on the diameter of the specimen, but on some intrinsic parameter of the material. In the case of the S series specimens, the edge effect affects a higher percentage of the cross-section and, by extension, a higher percentage of the pores. However, for the M series

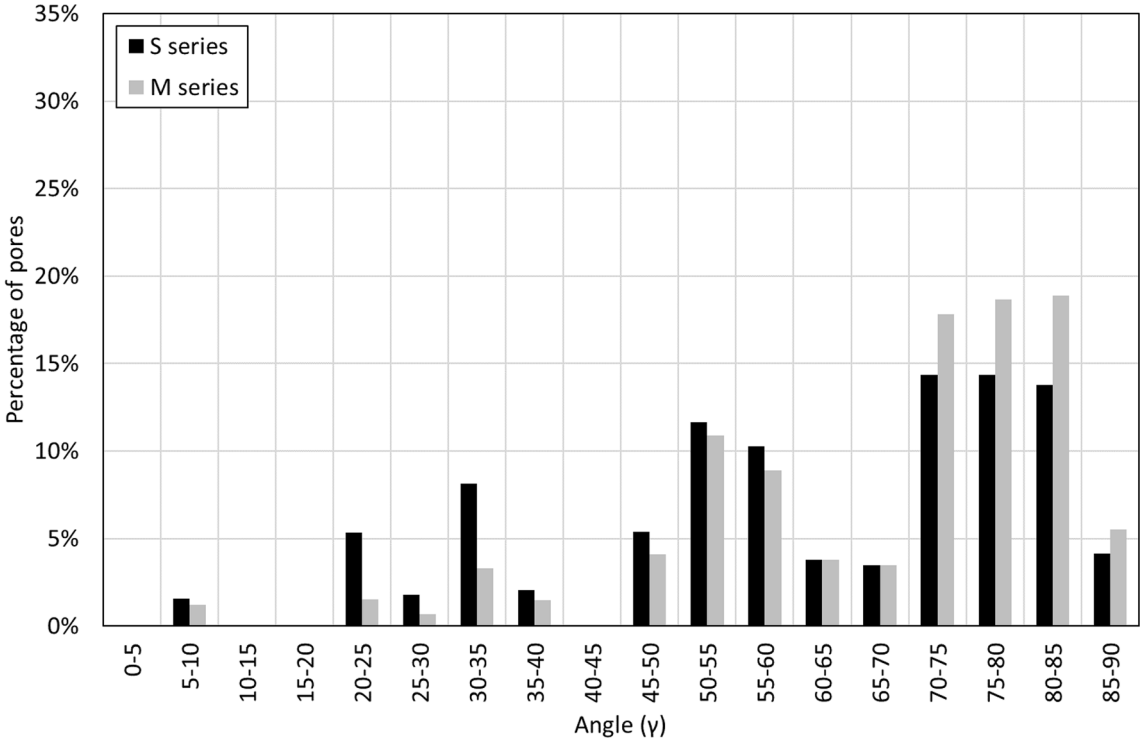

Fig. 17. Comparison of histograms of average pore orientations according to angle γ for series S and M.

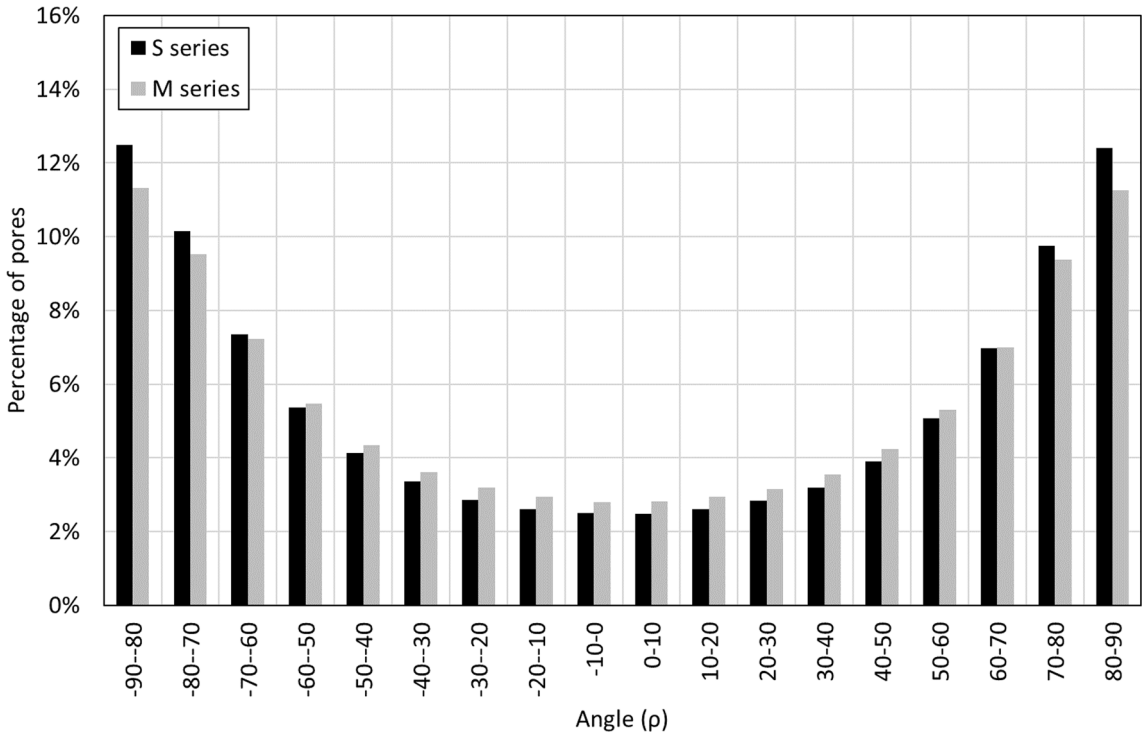

Fig. 18. Comparison of histograms of average pore orientations according to radial angle ρ for series S and M.

Table 9
Efficiency indices of pore orientation according to the gamma and radial angles for series S and M.

Efficiency index	S series	M series
e_γ	0.28 [0.02]	0.19 [0.02]
e_ρ	0.30 [0.02]	0.33 [0.01]

specimens, the edge effect is smaller.

The pore and fiber orientation patterns are very similar. This means that, at least in part, the pore orientation is conditioned by the fiber orientation.

3.4. Study of the variation of the mesostructure between the material close to the walls and in the interior of the specimens

As indicated above, the reverse size effect observed in the static tests may be because the specimens show a different mesostructure in the portion of the material in contact with the molds during the batching process and the portion which is far enough from the walls. Moreover, this difference is also size-dependent.

For this purpose, an in-depth study focused on how the mesostructure of the specimens varies between the inner and the outer sections is performed. In particular, the study will focus on the pores.

Firstly, once the centroids of all the pores of the specimen are known, a circumferential test is carried out on them [60]. In short, the circumferential test consists of determining, for each of the pores, its distance from the vertical axis of the specimen and, from this data, drawing the histogram of the distribution of this parameter. Fig. 19 shows the results obtained. The abscissa axis is the distance to the vertical axis of the cylinder relative to its radius, while the ordinate axis represents the volume of pores within each range in the *x*-axis divided by the volume of pores in the specimen (actually, in Fig. 19 the values refer to the average of a series of specimens). For instance, the average volume of pores in the M cylinders between 0.40 R and 0.45 R (R being the radius of the cylinder) divided by the volume of pores in the M cylinders is roughly 0.04. The theoretical curve is the one corresponding to a uniform pore distribution.

Fig. 19 shows how that the pore content is reduced at the outer tube. The wall effect in the S cylinders starts roughly at 0.175 R from the wall (R being the radius of the cylinder), the thickness of the tube being approximately 6.6 mm, whereas in the M cylinders, it starts at 0.125 R, resulting in a thickness of about 6.2 mm. Thus, we notice some wall effects roughly at 6 mm to 7 mm of the wall in two different sizes, i.e., the thickness of the layer affected by the wall effect does not depend on the size but likely on the fiber length, which is the same for the two sizes (13 mm). Moreover, this indicates that, in the case of the S series, 32% of the total section of the specimen belongs to the outer tube, while for the M series, this percentage is reduced to 24% (and to 16% for the L cylinders for a constant 6.5 mm-thick layer).

Second, the basic parameters of the porosity of the outer tube were compared with the average value of the entire specimen. As mentioned before, in the case of the S series, the outer tube has a thickness of 0.15d, whereas for the M series, the outer tube has a thickness of 0.075d.

The parameters to be analyzed are as follows:

1. Maximum pore size ($T_{max,pore}$), which corresponds to the pore length associated with an aggregate volume of 90% of the total.
2. Characteristic pore volume (V_{ch}), which corresponds to 90% of the total volume, that is, the one associated with the maximum pore size.
3. Characteristic porosity (p_{ch}), which is the ratio of the pore volume to the volume of the specimen (or tube).
4. Characteristic pore number (N_{pores}), which is the number of pores containing 90% of the total volume.
5. Characteristic pore density (p_d), which is the ratio of the number of pores to the volume of the test tube (or tube).
6. Average pore volume (PV_m), which is the ratio of the characteristic pore volume to the characteristic pore number.

Tables 10 to 15 present the results of the aforementioned parameters for both series S and M and for the entire specimen and outer tube.

Tables 10–15 display some interesting results. In both series, the characteristic porosity of the tube is lower than that of the entire

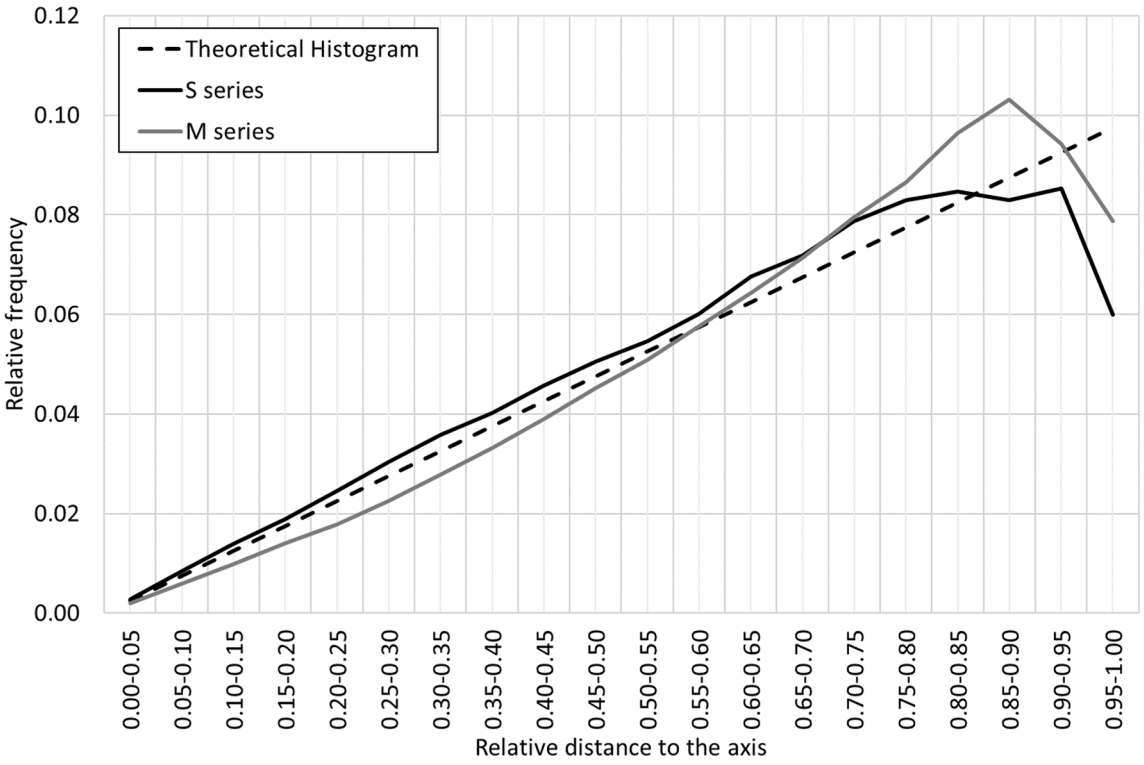

Fig. 19. Average values in the circumferential test.

Table 10
Main pore-related parameters for the S series cylinders (the entire specimen).

Specimen	$T_{max,pore}$ (mm)	V_{ch} (mm^3)	p_{ch} (%)	N_{pores}	p_d (mm^{-3})	PV_m (mm^3)
S-02	3.69	16,819	2.54	89,098	0.1345	0.1888
S-03	6.43	12,512	1.89	29,176	0.0440	0.4288
S-04	5.06	15,748	2.38	42,374	0.0639	0.3716
S-05	6.28	13,347	2.01	37,642	0.0568	0.3546
S-08	3.74	9201	1.39	31,638	0.0477	0.2908
S-12	4.54	12,539	1.89	46,780	0.0706	0.2680
S-15	5.57	12,700	1.92	22,212	0.0335	0.5717
μ	5.05	13,267	2.00	42,703	0.0644	0.3535
σ	1.12	2474	0.37	22,061	0.0333	0.1238
CV (%)	22	19	19	52	52	35

Table 11
Main pore-related parameters for the S series cylinders (the outer tube).

Specimen	$T_{max,pore}$ (mm)	V_{ch} (mm^3)	p_{ch} (%)	N_{pores}	p_d (mm^{-3})	PV_m (mm^3)
S-02	2.94	3050	1.66	20,185	0.1098	0.1511
S-03	11.71	3024	1.64	6912	0.0376	0.4375
S-04	11.14	3329	1.81	9139	0.0497	0.3642
S-05	12.49	3490	1.90	8791	0.0478	0.3970
S-08	3.47	1969	1.07	7429	0.0404	0.2650
S-12	6.16	3063	1.67	11,208	0.0609	0.2733
S-15	5.03	2328	1.27	4649	0.0253	0.5008
μ	7.56	2893	1.57	9759	0.0531	0.3413
σ	4.10	546	0.30	5029	0.0273	0.1190
CV (%)	54	19	19	52	0.52	35

Table 12
Comparison between the entire specimen and the outer tube for the S series cylinders.

Specimen	$p_{ch,outer\_tube}$ / $p_{ch,entire\_specimen}$	$p_{d,outer\_tube}$ / $p_{d,entire\_specimen}$
S-02	0.65	0.82
S-03	0.87	0.85
S-04	0.76	0.78
S-05	0.94	0.84
S-08	0.77	0.85
S-12	0.88	0.86
S-15	0.66	0.75
μ	0.79	0.82
σ	0.11	0.04
CV (%)	14	5

Table 13
Main pore-related parameters for the M series cylinders (the entire specimen).

Specimen	$T_{max,pore}$ (mm)	V_{ch} (mm^3)	p_{ch} (%)	N_{pores}	p_d (mm^{-3})	PV_m (mm^3)
M-01	5.86	22,806	1.45	68,052	0.0433	0.3351
M-02	5.87	40,360	2.57	104,993	0.0668	0.3844
M-03	7.00	41,743	2.66	107,228	0.0683	0.3893
S-04	6.20	30,073	1.91	87,819	0.0559	0.3424
S-05	7.30	29,289	1.86	74,790	0.0476	0.3916
S-13	5.86	35,078	2.23	122,299	0.0779	0.2868
S-14	7.00	35,187	2.24	103,921	0.0662	0.3386
μ	6.44	33,505	2.13	95,586	0.0609	0.3526
σ	0.64	6636	0.42	19,399	0.0124	0.0383
CV (%)	10	20	20	20	20	11

specimen. Similarly, in both series, the characteristic pore density is lower than the average.

The ratio between the characteristic pore volume of the tube pores and the characteristic pore volume of the whole specimen in the S series is higher than that in the M series (0.79 vs. 0.70). However, the ratio between the characteristic density of the tube pores and the

Table 14
Main pore-related parameters for the M series cylinders (the outer tube).

Specimen	$T_{max,pore}$ (mm)	V_{ch} (mm^3)	p_{ch} (%)	N_{pores}	p_d (mm^{-3})	PV_m (mm^3)
M-01	8.48	1420	0.63	4494	0.0198	0.3159
M-02	4.52	3580	1.58	13,190	0.0582	0.2714
M-03	18.04	4376	1.93	14,117	0.0622	0.3100
S-04	6.65	3172	1.40	12,450	0.0549	0.2548
S-05	10.58	2096	0.92	5724	0.0252	0.3662
S-13	9.65	4944	2.18	21,478	0.0947	0.2302
S-14	18.68	4667	2.06	16,035	0.0707	0.2911
μ	10.94	3465	1.53	12,498	0.0551	0.2914
σ	5.44	1330	0.59	5862	0.0259	0.0448
CV (%)	50	38	38	47	47	15

Table 15
Comparison between the entire specimen and the outer tube for the M series cylinders.

Specimen	$p_{ch,outer\_tube}$ / $p_{ch,entire\_specimen}$	$p_{d,outer\_tube}$ / $p_{d,entire\_specimen}$
M-01	0.43	0.46
M-02	0.61	0.87
M-03	0.73	0.91
S-04	0.73	0.98
S-05	0.50	0.53
S-13	0.98	1.22
S-14	0.92	1.07
μ	0.70	0.86
σ	0.20	0.28
CV (%)	29	32

characteristic density of the pores of the entire specimen in the S series is lower than that in the M series (0.82 vs. 0.86). When the average pore sizes were compared, it was observed that, in the S series, the average pore size of the outer tube is almost equal to that of the entire specimen. However, in the M series, the average pore size in the outer tube is clearly smaller than that of the entire specimen. The results show that the outer tube of the M series specimens has a proportionally lower porosity than that of the S series specimens, and it has smaller pores. This lower percentage of pores for the outer tube of the M series can lead to a higher strength for the outer tube, thereby increasing the compressive strength of the specimen. In contrast, in the S series specimens, the porosity parameters of the outer tube are more similar to those of the entire specimen, so the outer tube does not provide extra mechanical strength. This fact justifies the inverse size effect observed for the compressive strength given in Table 2. In other words, cylinders of different sizes contain non-identical internal mesostructure distributions. This distinction can be attributed to the wall effect during casting. In contrast, the cubic specimens cut from prisms maintained the same internal mesostructure for cubes of different sizes, as shown in a recent study by Ortega et al. [38].

The effect of the heterogeneities on fatigue is likely to be similar to the one observed on the monotonic strength because it is the limit behavior of fatigue when N tends to 1 [14]. However, cylinders of the S series endure more cycles than those of the M and L series, which may be due to other counteracting factors such as the statistical distribution of large pores or fatigue-induced maturation. In addition, as the range of the cyclic loads is proportional to the compressive strength for each series, the maximum and minimum absolute stress levels are higher for taller sizes, which may be another cause of the observed fatigue size effect.

4. Conclusions

The aim of this study is to analyze the influence of the concrete mesostructure on the size effect under compressive fatigue loading. For this purpose, an experimental study was carried out on cylindrical specimens of three different sizes made of steel fiber–reinforced concrete. The specimens were subjected to cyclic uniaxial compressive tests, and their deformations were monitored. The specimens were previously scanned by CT, and after post-processing the images, the individual parameters of the pores (length, volume, etc.) were obtained, as well as the orientation of the fibers. Based on the investigation, some interesting correlations between the mesostructure of the concrete and the size effect on fatigue were established.

The main conclusions are given below:

- The specimen size has a clear influence on the fatigue strength. Smaller specimens (S series) have a longer fatigue life than the rest (M and L series), with a difference of two orders of magnitude. Therefore, there is a size effect associated with fatigue life. This concurs with recent results on cubes made of the same fiber concrete [38], although cubes have longer lives than cylinders. The two sets of results, all specimens being of the same material and obtained with the same fatigue range, cover seven orders of magnitude in terms of fatigue life (only three for the average values), which indicates the importance of assessing the influence of each factor (size and shape of the specimens, mesostructure, fatigue-induced maturation, etc.) on the fatigue life.
- The specimen size also influences the quasi-static compressive strength but in the opposite direction. This inverse size effect in monotonic compression was verified by the decrease in porosity close to the cylindrical surfaces with size. In fact, the cylinders have an outer tube (whose thickness depends on the fiber length and cylinder size) in which the porosity is lower than that in the core of the cylinders.
- The relationship between the secondary strain rate ($d\varepsilon/dN$) and fatigue life is not affected by the size effect. Therefore, this relationship is intrinsic to the material. Other research works also prove that this relationship does not depend on the test frequency and fiber content in the case of fiber-reinforced concrete.
- Smaller specimens have smaller and less elongated pores, whereas larger specimens have somewhat larger and less rounded pores. However, the differences are small, and it is not possible to establish correlations between the pore shape and response under fatigue loading.
- The fatigue size effect depends on several phenomena, which in turn are determined by the material mesostructure and size of the specimen.
  - o The cumulative pore size curves and porosity curves reveal that the cylinder size influences the pore morphology because larger specimens have larger pores. A well-known mechanism of concrete failure in compression is microcrack propagation from the pores. Larger pores are more prone to this failure, being more vulnerable to cyclic compressive loading, which results in a shorter fatigue life. These large and weak pores in taller cylinders should also lead to a conventional statistical size effect in static compression. However, the wall effect seems to be the dominant factor that leads to the static inverse size effect.
  - o The inverse size effect in static compression may have a twofold influence on fatigue behavior. On the one hand, the absolute minimum and maximum loads in each cycle are smaller for small cylinders, which may support the finding that they have longer lives. On the other hand, larger cylinders should resist more cycles owing to their higher static strength. Nevertheless, such an effect is counteracted by other factors that also depend on the size.
  - o It is likely that, as in the cubes in [38], fatigue maturation may occur, especially in the small specimens. This may also support the finding that the small specimens resist more cycles.

The results of this study reveal that the size effect on fiber-reinforced

concrete cylinders loaded in compressive fatigue is partially due to the mesostructure of the concrete and, more particularly, to the distribution and size of the pores. However, further investigations on the several causes of the size effect of this material, especially on the effect of the geometry of the specimen on the fatigue behavior, are still necessary.

Declaration of Competing Interest

The authors declare that they have no known competing financial interests or personal relationships that could have appeared to influence the work reported in this paper.

Data availability

Data will be made available on request.

Acknowledgments

The authors are grateful for the financial support from the *Ministerio de Economía y Competitividad*, Spain with grant nos. PID2019-110928RB-C32, PID2019–110928RB–C31, and RTC–2017–6736–3, and from the *Junta de Comunidades de Castilla-La Mancha*, Spain through grant no. SBPLY/19/180501/000220.

References

[1] Poveda E, Yu RC, Lancha JC, Ruiz G. A numerical study on the fatigue life design of concrete slabs for railway tracks. Eng Struct 2015;100:455–67.
[2] American Concrete Institute. (2016). "Report on Design of Concrete Wind Turbines" ACI ITG-9R-16, Farmington Hills, MI, USA.
[3] Lee MK, Barr BIG. An overview of the fatigue behaviour of plain and fibre reinforced concrete. Cem Concr Compos 2004;26(4):299–305.
[4] di Prisco M, Pizzari G, Vandewalle L. Fibre reinforced concrete: new design perspectives. Mater Struct 2009;42:1261–81.
[5] Barros J, Sanz B, Kabele P, Yu RC, Meschke G, Planas J, et al. Competición a ciegas de simulaciones numéricas del fallo a cortante de vigas de hormigón reforzado con fibras. Hormigón y Acero 2022;73(296):17–39.
[6] De La Rosa Á, Ruiz G, Poveda E. Study of the Compression Behavior of Steel-Fiber Reinforced Concrete by Means of the Response Surface Methodology. Applied Sciences 2019;9(24):5330. https://doi.org/10.3390/app9245330.
[7] Ruiz G, De La Rosa Á, Poveda E. Relationship between residual flexural strength and compression strength in steel-fiber reinforced concrete within the new Eurocode 2 regulatory framework. Theor Appl Fract Mech 2019;103:102310.
[8] Ruiz G, De La Rosa Á, Wolf S, Poveda E. Model for the compressive stress–strain relationship of steel fiber-reinforced concrete for non-linear structural analysis. Hormigón y Acero 2018;69(S1):75–80.
[9] Barros JAO, Cunha VMCF, Ribeiro AF, Antunes JAB. Post-cracking behaviour of steel fibre reinforced concrete. Mater Struct 2005;38(1):47–56.
[10] Cachim PB, Figueiras JA, Pereira PAA. Fatigue behavior of fiber-reinforced concrete in compression. Cem Concr Compos 2002;24(2):211–7.
[11] Cornelissen H, Reinhardt HW. Uniaxial tensile fatigue failure of concrete under constant-amplitude and program loading. Mag Concr Res 1984;36(129):216–26.
[12] Singh SP, Kaushik SK. Flexural fatigue life distributions and failure probability of steel fibrous concrete. ACI Mater J 2000;97(6):658–67.
[13] Medeiros A, Zhang XX, Ruiz G, Yu RC, Velasco MDSL. Effect of the loading frequency on the compressive fatigue behavior of plain and fiber reinforced concrete. Int J Fatigue 2015;70:342–50.
[14] Saucedo L, Yu RC, Medeiros A, Zhang XX, Ruiz G. A probabilistic fatigue model based on the initial distribution to consider frequency effect in plain and fiber reinforced concrete. Int J Fatigue 2013;48:308–18.
[15] Poveda E, Ruiz G, Cifuentes H, Yu RC, Zhang XX. Influence of the fiber content on the compressive low-cycle fatigue behavior of self-compacting SFRC. Int J Fatigue 2017;101:9–17.
[16] Vicente MA, González DC, Mínguez J, Tarifa M, Ruiz G, Hindi R. Influence of the pore morphology of high strength concrete on its fatigue life. Int J Fatigue 2018;112:106–16.
[17] Vicente MA, Mínguez J, González DC. Computed tomography scanning of the internal microstructure, crack mechanisms, and structural behavior of fiber-reinforced concrete under static and cyclic bending tests. Int J Fatigue 2019;121:9–19.
[18] Vicente MA, Ruiz G, González DC, Mínguez J, Tarifa M, Zhang X. Effects of fiber orientation and content on the static and fatigue behavior of SFRC by using CT-Scan technology. Int J Fatigue 2019;128.
[19] Tarifa M, Ruiz G, Poveda E, Zhang XX, Vicente MA, González DC. Effect of uncertainty on load position in the fatigue life of steel-fiber reinforced concrete under compression. Mater Struct 2018;51:31.
[20] Ortega JJ, Ruiz G, Yu RC, Afanador-García N, Tarifa M, Poveda E, et al. Number of tests and corresponding error in concrete fatigue. Int J Fatigue 2018;116:210–9.
[21] Blasón S, Poveda E, Ruiz G, Cifuentes H, Fernández Canteli A. Twofold normalization of the cyclic creep curve of plain and steel-fiber reinforced concrete and its application to predict fatigue failure. Int J Fatigue 2019;120:215–27.
[22] Blasón S, Fernández Canteli A, Poveda E, Ruiz G, Yu RC, Castillo E. Damage evolution and probabilistic strain-lifetime assessment of plain and fiber-reinforced concrete under compressive fatigue loading: Dual and integral phenomenological model. Int J Fatigue 2022;158:106739.
[23] Bažant ZP, Planas J. Fracture and size effect in concrete and other quasibrittle materials. Boca Raton, Florida, USA: CRC Press; 1998.
[24] Del Viso JR, Carmona JR, Ruiz G. Shape and size effects on the compressive strength of high-strength concrete. Cem Concr Res 2008;38(3):386–95.
[25] Castillo E, Fernandez-Canteli A. A Unified Statistical Methodology for Modeling Fatigue Damage. Netherlands, Dordrecht: Springer; 2009.
[26] Sinaie S, Heidarpour A, Zhao XL, Sanjayan JG. Effect of size on the response of cylindrical concrete samples under cyclic loading. Constr Build Mater 2015;84:399–408.
[27] Bažant ZP. Instability, ductility and size effect in strain-softening concrete. J Eng Mech Division-ASCE 1976;102(2):331–44.
[28] Tanigawa Y, Yamada K. Size effect in compressive strength of concrete. Cem Concr Res 1978;8(2):181–90.
[29] Mindess S. The effect of specimen size on the fracture energy of concrete. Cem Concr Res 1984;14(3):431–6.
[30] Jansen DC, Shah SP. Effect of length on compressive strain softening of concrete. J Eng Mech-ASCE 1997;123(1):25–35.
[31] Sim JI, Yang KH, Jeon JK. Influence of aggregate size on the compressive size effect according to different concrete types. Constr Build Mater 2013;44:716–25.
[32] Alam SY, Zhu R, Loukili A. A new way to analyse the size effect in quasi-brittle materials by scaling the heterogeneity size. Eng Fract Mech 2020;225.
[33] Bažant ZP, Xu KM. Size effect in fatigue fracture of concrete. ACI Mater J 1991;88(4):390–9.
[34] Slowik V, Plizzari GA, Saouma VE. Fracture of concrete under variable amplitude fatigue loading. ACI Mater J 1996;93(3):272–83.
[35] Le JL, Bažant ZP. Unified nano-mechanics based probabilistic theory of quasibrittle and brittle structures: II. Fatigue crack growth, lifetime and scaling. J Mech Phys Solids 2011;59(7):1322–37.
[36] Ray S, Kishen JMC. Fatigue crack propagation model and size effect in concrete using dimensional analysis. Mech Mater 2011;43(2):75–86.
[37] Kirane K, Bažant ZP. Size effect in Paris law and fatigue lifetimes for quasibrittle materials: Modified theory, experiments and micro-modeling. Int J Fatigue 2016;83(2):209–20.
[38] Ortega JJ, Ruiz G, Poveda E, González DC, Tarifa M, Zhang XX, Yu RC, Vicente MA, De la Rosa A, Garijo L. Size effect on the compressive fatigue of fibre-reinforced concrete. Construct Build Mater 2022;322.
[39] Taher SEDF, Fawzy TM. Performance of very-high-strength concrete subjected to short-term repeated loading. Mag Concr Res 2000;52(3):219–23.
[40] Liu D, Šavija B, Smith GE, Flewitt PEJ, Lowe T, Schlangen E. Towards understanding the influence of porosity on mechanical and fracture behaviour of quasi-brittle materials: experiments and modelling. Int J Fract 2017;205(1):57–72.
[41] Luo Q, Liu DX, Qiao P, Feng QG, Sun LZ. Microstructural damage characterization of concrete under freeze-thaw action. Int J Damage Mech 2018;27(10):1551–68.
[42] Zhang S, Cao K, Wang C, Wang X, Deng G, Wei P. Influence of the porosity and pore size on the compressive and splitting strengths of cellular concrete with millimeter-size pores. Constr Build Mater 2020;235.
[43] Rózanski A, Rajczakowska M, Serwicki A. The influence of microstructure geometry on the scale effect in mechanical behaviour of heterogeneous materials. Sci Eng Compos Mater 2017;24:557–71.
[44] Wang X, Yang Z, Jivkov AP. Monte Carlo simulations of mesoscale fracture of concrete with random aggregates and pores: a size effect study. Constr Build Mater 2015;80:262–72.
[45] Skarżyński Ł, Suchorzewski J. Mechanical and fracture properties of concrete reinforced with recycled and industrial steel fibers using Digital Image Correlation technique and X-ray micro computed tomography. Constr Build Mater 2018;183:283–99.
[46] Gao J, Sha A, Wang Z, Hu L, Yun D, Liu Z, et al. Characterization of carbon fiber distribution in cement-based composites by Computed Tomography. Constr Build Mater 2018;177:134–47.
[47] Mínguez J, Vicente MA, González DC. Pore morphology variation under ambient curing of plain and fiber-reinforced high performance mortar at an early age. Constr Build Mater 2019;198:718–31.
[48] Vicente MA, Ruiz G, González DC, Mínguez J, Tarifa M, Zhang XX. CT-Scan study of crack patterns of fiber-reinforced concrete loaded monotonically and under low-cycle fatigue. Int J Fatigue 2018;114:138–47.
[49] Suzuki T, Shiotani T, Ohtsu M. Evaluation of cracking damage in freeze-thawed concrete using acoustic emission and X-ray CT image. Constr Build Mater 2017;136:619–26.
[50] Man H-K, Mier JGM. Size effect on strength and fracture energy for numerical concrete with realistic aggregate shapes. Int J Fract 2008;154(1-2):61–72.
[51] Man H-K, van Mier JGM. Damage distribution and size effect in numerical concrete from lattice analyses. Cem Concr Compos 2011;33(9):867–80.
[52] Suchorzewski J, Tejchman J, Nitka M, Bobiński J. Meso-scale analyses of size effect in brittle materials using DEM. Granular Matter 2019;21:9.
[53] Dhaheer MSA, Al-Rubaye MM, Alyhya WS, Karihaloo BL, Kulasegaram S. Proportioning of self-compacting concrete mixed based on target plastic viscosity and compressive strength: Part I - Mix design procedure. J. Sustain. Cem.-Based Mater. 2016;4:199–216.

[54] De La Rosa Á, Poveda E, Ruiz G, Cifuentes H. Proportioning of self-compacting steel-fiber reinforced concrete mixes based on target plastic viscosity and compressive strength: Mix-design procedure & experimental validation. Constr. Build. Mater. 2018;189:409–19.
[55] BS EN 12350-8. Testing Fresh Concrete. Self-Compacting Concrete. Slump-Flow Test, BSI; 2010.
[56] UNE-EN 12390-3. Ensayos de hormigón endurecido. Parte 3: Determinación de la resistencia a compresión de probetas; 2020.
[57] Vicente MA, González DC, Mínguez J. Recent advances in the use of computed tomography in concrete technology and other engineering fields. Micron 2019; 118:22–34.
[58] Vicente MA, Mínguez J, González DC. The Use of Computed Tomography to Explore the Microstructure of Materials in Civil Engineering: From Rocks to Concrete. In: Mesrur-Halefoğlu A. (Ed.), Comput. Tomogr. - Adv. Appl., InTech, pp. 207–229; 2017.
[59] Mena A, González DC, Mínguez J, Vicente MA. Computed tomography beyond medicine: Applications to the microstructural study of concrete and other engineering materials. Hormigón y Acero 2020;71(292):e1–12.
[60] Vicente MA, Mena A, Mínguez J, González DC. Use of Computed Tomography Scan Technology to Explore the Porosity of Concrete: Scientific Possibilities and Technological Limitations. Appl Sci 2021;11:8699.
[61] Le J-L, Bažant ZP, Bazant MZ. Unified nano-mechanics based probabilistic theory of quasibrittle and brittle structures: I. Strength, static crack growth, lifetime and scaling. J Mech Phys Solids 2011;59:1291–321.
[62] Sparks PR, Menzies JB. The effect of rate of loading upon the static and fatigue strengths of plain concrete in compression. Mag Concr Res 1973;25(83):73–80.
[63] Chen C, Chen X, Zhang J. Experimental study on flexural fatigue behavior of self-compacting concrete with waste tire rubber. Mech Adv Mater Struct 2021;28(16): 1691–702.
[64] Huang B-T, Li Q-H, Xu S-L, Zhou B-M. Frequency Effect on the Compressive Fatigue Behavior of Ultrahigh Toughness Cementitious Composites: Experimental Study and Probabilistic Analysis. J Struct Eng 2017;143:04017073.
[65] González DC, Mena Á, Mínguez J, Vicente MA. Influence of air-entraining agent and freeze-thaw action on pore structure in high-strength concrete by using CT-Scan technology. Cold Reg Sci Technol 2021;192.
[66] Krause M, Hausherr JM, Burgeth B, Herrmann C, Krenkel W. Determination of the fibre orientation in composites using the structure tensor and local X-ray transform. J Mater Sci 2010;45(4):888–96.